MOX-Report No. 28/2018

Segregated algorithms for the numerical simulation of cardiac electromechanics in the left human ventricle

Gerbi, A.; Dede', L.; Quarteroni, A.

MOX, Dipartimento di Matematica
Politecnico di Milano, Via Bonardi 9 - 20133 Milano (Italy)

mox-dmat@polimi.it http://mox.polimi.it

Segregated algorithms for the numerical simulation of cardiac electromechanics in the left human ventricle

A. Gerbi*[1], L. Dede'[2], and A. Quarteroni[1,2]

[1]Institute of Mathematics, École Polytechnique Fédérale de Lausanne,
Avenue Piccard, CH-1015, Lausanne, Switzerland
[2]Modeling and Scientific Computing (MOX), Mathematics Department,
Politecnico di Milano, Piazza Leonardo da Vinci 32, 20133, Milan, Italy

Abstract

In this paper, we propose and numerically assess three segregated algorithms for the numerical solution of the coupled electromechanics problem for the left human ventricle. We split the coupled problem into its core mathematical models and we proceed to their numerical approximation. Space and time discretizations of the core problems are carried out by means of the Finite Element Method and Backward Differentiation Formulas, respectively. In our mathematical model, electrophysiology is represented by the monodomain equation while the Holzapfel-Ogden strain energy function is used for the passive characterization of tissue mechanics. A transmurally variable active strain model is used for the active deformation of the fibers of the myocardium to couple the electrophysiology and the mechanics in the framework of the active strain model. In this work we focus on the numerical strategy to deal with the solution of the coupled model, which is based on novel segregated algorithms that we propose. These also allow using different time discretization schemes for the core submodels, thus leading to the formulation of staggered algorithms, a feature that we sistematically exploit to increase the overall efficiency of the computational procedure. We assess the accuracy of these segregated algorithms, measured by means of numerical tests, which exhibit at least first order of accuracy. We take advantage of the efficiency of the segregated schemes to solve, in an High Performance Computing framework, the cardiac electromechanics problem for the human left ventricle, for both idealized and subject-specific configurations.

1 Introduction

The heart performs two simple, fundamental, tasks: it pumps the deoxygenated blood to the lungs to get oxygen and release carbon dioxide, while it simultaneously pushes the

---

*Corresponding Author: antonello.gerbi@epfl.ch

oxygen rich blood into the arteries delivering it to tissues and organs [46]. Its function, however, is the result of several physical processes taking place at different spatial scales, i.e. at the cellular, tissue, and organ levels. In the mathematical modeling of the heart function all these processes have to be properly considered and, above all, properly integrated; we refer to this as an "integrated heart model" [60]. The electrophysiology, the active and the passive mechanics are referred to as "single core models", and are expressed by systems of Ordinary Differential Equations (ODEs) and Partial Differential Equations (PDEs). Although their individual behavior is nowadays quite established, further theoretical studies are necessary to better understand their interactions [12, 19, 26, 28, 61, 66]. Since the processes under consideration feature different spatial and temporal scales, the grid for the numerical approximation of the individual core models must be properly chosen. Moreover, the discretized integrated problem can be formulated by either a *monolithic* approach, where the approximated equations are assembled in a single large system and simultaneously solved, or a *segregated* approach, where the approximated equations are solved sequentially.

We focus here on the electromechanics of the left ventricle (LV). For the investigation of this model and its numerical approximation see, e.g., in [33, 53, 60, 61, 67, 76, 79, 80]. Segregated algorithms are investigated in [4, 12, 33, 44, 67, 80], where the electrophysiology and the mechanics problems are solved separately. In [20, 21, 37], the integrated problem is instead solved using a monolithic approach. In either case, suitable solvers (and preconditioners) must be employed for the efficient solution of the linear systems stemming from the discretization of the problems.

In this work, we use the monodomain equation [13, 41, 59] together with the minimal Bueno-Orovio ionic model [8] for the description of the electrophysiology. For the passive mechanics, we use the popular Holzapfel-Ogden model [39] together with the active strain approach [2, 3] for the active mechanics, the latter endowed with a newly proposed model for the transmurally heterogeneous thickening of the myocardium [6]. The mechanics is then coupled with the electrophysiology by means of a mathematical model describing the shortening of the myocardial fibers [28, 70], triggered by a change in the ionic concentrations in the cardiac cells, namely the intracellular calcium concentration. Regarding the numerical approximation of the integrated model, we use the Finite Element Method (FEM) for the space discretization while the time discretization is carried by means of the Backward Differentiation Formulas (BDFs) [62]. We propose three novel segregated algorithms in combination with both implicit and semi-implicit schemes, the latter consisting in the partial evaluation of the nonlinear terms with an approximation of the unknowns of the same order of the BDF scheme [11, 29]. We compare the numerical results obtained by means of the segregated algorithms with those of the monolithic method proposed in [28] for physically meaningful benchmark problems. We develop our segregated algorithms in a way such that different timestep sizes for the electrophysiology and the mechanics can be used, thus leading to the so-called *staggered* algorithms. The use of different timestep sizes for the time discretization of the single core models is indeed made straightforward by the use of segregated approaches. Moreover, this is physically motivated as each core model features very different time scales: namely, the electrophysiology requires a small timestep size while the mechanics yields stable and accurate results also for relatively coarse time discretizations. We show that the segregated schemes are accurate of order one. Moreover, regarding the computational efficiency, we show that the segregated algorithms allow dramatic reductions of the computational costs with respect to the monolithic scheme. This is particularly true for a segregated algorithm in which the ionic, the monodomain, the mechanical activation, and the mechanics equations are fully decoupled and a timestep size ten times larger is used for the latter with respect to the former. Finally, we use the proposed algorithms for subject-specific large scale simulations for a full heartbeat and discuss the results thus obtained.

This paper is organized as follows: in Section 2 we recall the mathematical models for the electrophysiology, the mechanics and the mechanical activation of the myocardium; in Section 3 we carry on the space and time discretizations of the single core models; in Section 4 we propose the segregated algorithms for the solution of the integrated problem; in Section 5 we report and discuss the numerical results obtained with the proposed methods; finally, we draw our Conclusions.

2 Mathematical models

We recall, for each physical process, the underlying mathematical models in the form of ODEs and PDEs.

2.1 Ionic model and monodomain equation

The systolic phase of the LV starts when the electric signal originated from the atrioventricular node is conveyed through the Purkinje fibers network and delivered to the myocardium [7, 15, 38, 55]. The signal triggers a complex interaction between the transmembrane potential v and different ionic species thus causing a quick depolarization and repolarization of the cells. This change of v is known as *action potential* [47]. The electric signal propagates faster along the myocardial fibers which, together with the sheets, characterizes the internal structure of the muscle [72] as depicted in Figure 1.

We use a set of N_I ODEs in the ionic variables $\mathbf{w} = \{w_q\}_{q=1}^{N_I}$ to model the ionic species concentrations and currents through the cell membrane and the *monodomain equation*, a nonlinear diffusion-reaction parabolic equation derived from the bidomain equations under simplifying assumptions [13, 15], to model the tissue electrophysiology. This is compactly

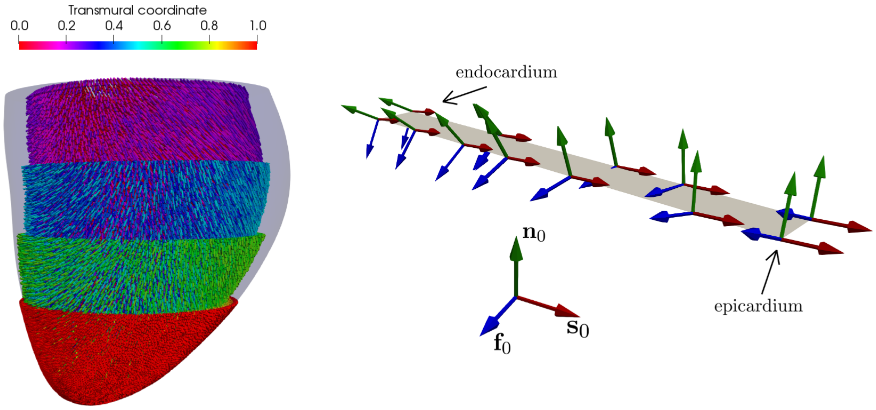

Figure 1: Fibers in a subject-specific geometry (left) colored by a transmurally linear variable and a close up of a slice with fibers $\mathbf{f}_0$, sheets $\mathbf{s}_0$, and normals $\mathbf{n}_0$, together with their relative position (right).

written as:

$$\begin{cases} \dfrac{\partial \mathbf{w}}{\partial t} = \boldsymbol{\alpha}(v)(\mathbf{w}^{\infty}(v) - \mathbf{w}) + \boldsymbol{\beta}(v)\mathbf{w} & \text{in } \Omega_0 \times (0,T), \\ \chi\left(C_m \dfrac{\partial v}{\partial t} + I^{ion}(v,\mathbf{w})\right) = \nabla \cdot (J\mathbf{F}^{-1}\mathbf{D}_m\mathbf{F}^{-T}\nabla v) + I^{app}(t) & \text{in } \Omega_0 \times (0,T), \\ (J\mathbf{F}^{-1}\mathbf{D}_m\mathbf{F}^{-T}\nabla v) \cdot \mathbf{N} = 0 & \text{on } \partial\Omega_0 \times (0,T), \\ v = v_0, \quad \mathbf{w} = \mathbf{w}_0 & \text{in } \Omega_0 \times \{0\}, \end{cases} \tag{1}$$

Here, Ω_0 is the reference domain and $T > 0$ is the final time of the simulation; χ and $C_m \in \mathbb{R}^+$ are the ratio of membrane surface with respect to the volume and the membrane capacitance, respectively. The term $I^{ion}(v, \mathbf{w})$ represents the currents driven by the ions concentrations while I^{app} is an externally applied stimulus. The current geometry displacement (the displacement of the myocardium) $\mathbf{d} = \mathbf{X} - \mathbf{x}$ determines $\mathbf{F} = \mathbf{I} + \dfrac{\partial \mathbf{d}}{\partial \mathbf{X}}$ and $J = \det(\mathbf{F})$, where $\mathbf{X}$ and $\mathbf{x}$ are the space variables in the reference (Ω_0) and in the deformed (Ω) configurations, respectively. We neglect, for simplicity, stretch activated currents (SAC) [22, 42] and other bioelectrical effects of mechanical feedbacks [14, 17, 18]. To account for the anisotropic electrical conductance of the myocardium, the diffusion tensor reads $\mathbf{D}_m = \sigma_{iso}(\mathbf{I} - \mathbf{f}_0 \otimes \mathbf{f}_0) + \sigma_f \mathbf{f}_0 \otimes \mathbf{f}_0$, where $\mathbf{f}_0$ is the local fiber orientation (see Figure 1) that varies transmurally, while the sheets direction $\mathbf{s}_0$ (which is oriented as the normal to the collagene sheets) is orthogonal to the LV walls. The $\mathbf{n}_0$ direction is orthogonal to both $\mathbf{f}_0$ and $\mathbf{s}_0$; σ_{iso} and σ_f are the fiber-transversal and the fiber-longitudinal conductances, respectively. Finally, the terms $\boldsymbol{\alpha}(v)$, $\boldsymbol{\beta}(v)$, and I^{ion} are prescribed according to the ionic model. Among the many models proposed in literature ([1, 47, 48, 52, 78]) we choose the Bueno-Orovio minimal model [8] for which $N_I = 3$. We assimilate the variable w_3 to the intracellular concentration $[Ca^{2+}]$.

2.2 Mechanical activation

The concentration of calcium ions $[Ca^{2+}]$ drives complex dynamics in the sarcomeres [65], which lead to the cardiomyocites stretching. We use a phenomenological model for the local shortening of the fibers (denoted by γ_f) at the macroscopic level. The latter, firstly proposed in [70], and further developed in [28, 67], reads:

$$\begin{cases} \dfrac{\partial \gamma_f}{\partial t} - \dfrac{\varepsilon}{g(w_3)} \Delta \gamma_f = \dfrac{1}{g(w_3)} \Phi(w_3, \gamma_f, \mathbf{d}) & \text{in } \Omega_0 \times (0, T), \\ \nabla \gamma_f \cdot \mathbf{N} = 0 & \text{on } \partial\Omega_0 \times (0, T), \\ \gamma_f = 0 & \text{in } \Omega_0 \times \{0\}. \end{cases} \tag{2}$$

Here $g(w_3) = \widehat{\mu}_A w_3^2$, while $\Phi(w_3, \gamma_f, \mathbf{d})$ depends on the sarcomere force-length relationship [34, 28, 67]; we refer the reader to [28] for the expression of $\Phi(w_3, \gamma_f, \mathbf{d})$. Finally, $\widehat{\mu}_A, \varepsilon \in \mathbb{R}^+$ are tuning parameters for the subject-specific case under study.

2.3 Passive and active mechanics

We model the myocardium as a hyperelastic material [54]; then $\mathbf{P} = \mathbf{P}(\mathbf{d}) = \frac{\partial \mathcal{W}}{\partial \mathbf{F}}$ is the first Piola-Kirchhoff stress tensor and $\mathcal{W}$ the strain energy density function. To model moderate volumetric changes (2-15%), we use the *nearly-incompressible* formulation [25] by multiplicatively decomposing the deformation gradient $\mathbf{F}$ into the isochoric $\overline{\mathbf{F}}$ and the volumetric $\mathbf{F}_v$ parts as $\mathbf{F} = \mathbf{F}_v \overline{\mathbf{F}}$, where $\mathbf{F}_v = J^{\frac{1}{3}} \mathbf{I}$. We use the Holzapfel-Ogden strain energy density function [39] – the state–of–the–art in passive myocardial tissue modeling – with a volumetric term weakly penalizing volumetric variations [73] $\mathcal{W}(\mathbf{C}, J) = \mathcal{W}_{el}(\mathbf{C}, J) + \mathcal{W}_{vol}(J)$, where the expression of $\mathcal{W}_{el}$ is given in [28] with parameters determined in [39] and $\mathcal{W}_{vol} = \frac{B}{2}(J-1)\log(J)$; $B \in \mathbb{R}^+$ is the *bulk modulus*.

We use the *active strain* formulation [2, 3, 51, 69] to account for the active behavior of the myocardium. This approach corresponds to a decomposition of $\mathbf{F}$ in the form $\mathbf{F} = \mathbf{F}_E \mathbf{F}_A = J^{\frac{1}{3}} \overline{\mathbf{F}}_E \mathbf{F}_A$; $\overline{\mathbf{F}}_E$ is the isochoric component of the elastic (passive) part of the deformation, where $\mathbf{F}_E = \mathbf{F}_v \overline{\mathbf{F}}_E$, and $\mathbf{F}_A$ is the prescribed active deformation (active strain) tensor. We have that $\mathbf{P} = \det(\mathbf{F}_A) \mathbf{P}_E \mathbf{F}_A^{-T}$, where $\mathbf{P}_E = \frac{\partial \mathcal{W}}{\partial \mathbf{F}_E}$. We refer to [28, 30, 31] for more details. We use the following orthotropic form for the tensor $\mathbf{F}_A$ [3, 5, 57, 67, 68]:

$$\mathbf{F}_A = \mathbf{I} + \gamma_f \mathbf{f}_0 \otimes \mathbf{f}_0 + \gamma_s \mathbf{s}_0 \otimes \mathbf{s}_0 + \gamma_n \mathbf{n}_0 \otimes \mathbf{n}_0,$$

where γ_n and γ_s are the local shortening (or elongation) of the tissue in the directions $\mathbf{s}_0$ and $\mathbf{n}_0$, respectively. Following [6, 28], we set γ_n as transmurally variable, $\gamma_n =$

$k'(\lambda)\left(\frac{1}{\sqrt{1+\gamma_f}}-1\right)$, where λ is a transmural coordinate, varying from λ_{endo} at the endocardium and λ_{epi} at the epicardium. The dependent variable γ_s is chosen to ensure $\det(\mathbf{F}_A)=1$; hence, $\gamma_n=\gamma_n(\gamma_f)$ and $\gamma_s=\gamma_s(\gamma_f)$.

We finally use the stress tensor $\mathbf{P}(\mathbf{d},\gamma_f)$ in the momentum equation:

$$\begin{cases} \rho\dfrac{\partial^2\mathbf{d}}{\partial t^2}-\nabla_0\cdot\mathbf{P}(\mathbf{d},\gamma_f)=\mathbf{0} & \text{in } \Omega_0\times(0,T), \\ (\mathbf{N}\otimes\mathbf{N})\left(K_\perp^\eta\mathbf{d}+C_\perp^\eta\dfrac{\partial\mathbf{d}}{\partial t}\right)+(\mathbf{I}-\mathbf{N}\otimes\mathbf{N})\left(K_\parallel^\eta\mathbf{d}+C_\parallel^\eta\dfrac{\partial\mathbf{d}}{\partial t}\right) & \\ \quad+\mathbf{P}(\mathbf{d},\gamma_f)\,\mathbf{N}=\mathbf{0} & \text{on } \Gamma_0^\eta\times(0,T), \\ \mathbf{P}(\mathbf{d},\gamma_f)\,\mathbf{N}=p^{endo}(t)\mathbf{N} & \text{on } \Gamma_0^{endo}\times(0,T), \\ \mathbf{d}=\mathbf{d}_0,\ \dfrac{\partial\mathbf{d}}{\partial t}=\dot{\mathbf{d}}_0 & \text{in } \Omega_0\times\{0\}. \end{cases} \tag{3}$$

where ρ is the density of the myocardium. The boundary $\partial\Omega_0$ is partitioned in Γ_0^{endo}, Γ_0^{epi}, and Γ_0^{base}, representing the endocardium, the epicardium, and the ventricle base, respectively. For $\eta\in\{base,epi\}$, we consider generalized Robin conditions with parameters $K_\perp^\eta,K_\parallel^\eta,C_\perp^\eta,C_\parallel^\eta\in\mathbb{R}^+$, whereas the pressure $p^{endo}(t)$ (still prescribed at this stage) is set at the endocardium; $\mathbf{d}_0$ and $\dot{\mathbf{d}}_0$ denote initial conditions.

2.3.1 Prestress

If, at the initial time $t=0$, $\overline{p}^{endo}=p^{endo}(0)>0$, the blood pressure acts at the endocardial walls and thus the net force acting on the myocardium is not zero. The reference configuration Ω_0 is therefore unstressed at $t=0$, which leads to unphysical deformations in problem (3). To overcome this issue, we use a *prestress* approach [40, 77] to determine the internal stresses of the myocardium such that the latter remains in mechanical equilibrium at $t=0$. After observing that $\mathbf{P}(\mathbf{d},\gamma_f)=\mathbf{P}(\mathbf{d}_0)$ at $t=0$, we look for a vector $\widehat{\mathbf{d}}_0$ and a tensor $\mathbf{P}_0$ such that

$$\begin{cases} \nabla_0\cdot\mathbf{P}(\widehat{\mathbf{d}}_0)=-\nabla_0\cdot\mathbf{P}_0 & \text{in } \Omega_0, \\ (\mathbf{N}\otimes\mathbf{N})K_\perp^\eta\widehat{\mathbf{d}}_0+(\mathbf{I}-\mathbf{N}\otimes\mathbf{N})K_\parallel^\eta\widehat{\mathbf{d}}_0+\mathbf{P}(\widehat{\mathbf{d}}_0)\,\mathbf{N}=\mathbf{0} & \text{on } \Gamma_0^\eta, \\ \mathbf{P}(\widehat{\mathbf{d}}_0)\,\mathbf{N}=\overline{p}^{endo}\mathbf{N} & \text{on } \Gamma_0^{endo}, \end{cases} \tag{4}$$

with $\widehat{\mathbf{d}}_0\approx\mathbf{d}_0$. We then use the stress tensor $\widetilde{\mathbf{P}}(\mathbf{d},\gamma_f)=\mathbf{P}(\mathbf{d},\gamma_f)+\mathbf{P}_0$ in place of $\mathbf{P}(\mathbf{d},\gamma_f)$ in the first of Eq. (3), and set $\mathbf{d}_0=\widehat{\mathbf{d}}_0$, $\dot{\mathbf{d}}_0=\mathbf{0}$. Since the pair $(\widehat{\mathbf{d}}_0,\mathbf{P}_0)$ is a solution of Eq. (4), this allows the myocardium to remain in mechanical equilibrium at $t=0$.

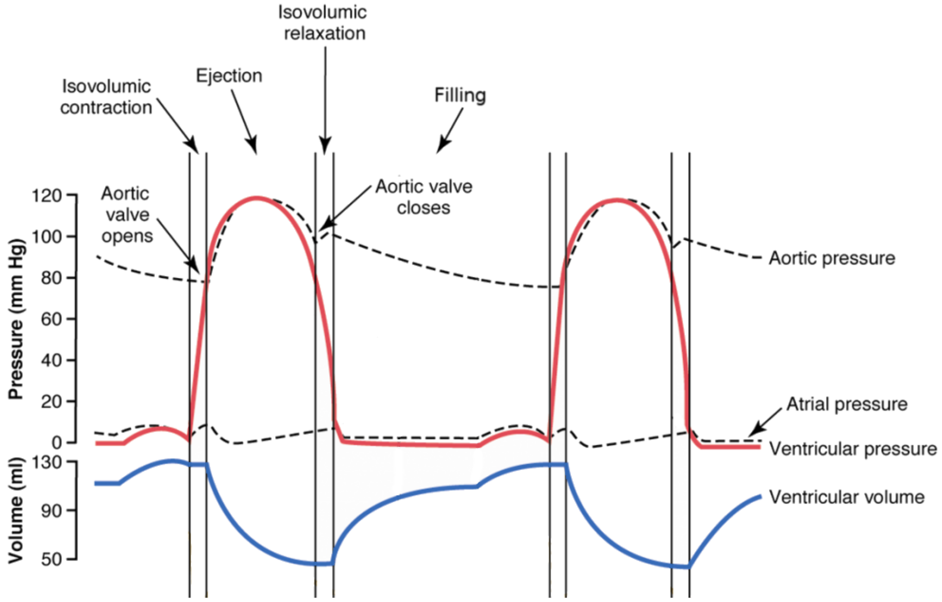

Figure 2: Wiggers diagram [43] of the left heart depicting the aortic, ventricular, and atrial pressures as well as the ventricular volume, along the four phases of the cardiac cycle.

2.4 Cardiac cycle

As we aim at modeling the LV electromechanics for a full heartbeat (tipically about 0.8 s long), we need to account for the blood interaction with the LV along the different phases of the heartbeat (see Figure 2). Hence, we solve different 0D model (ODEs) [26, 67, 80]. The phases are, in order:

1) Isovolumic contraction: the early stages of the LV contraction drive an increment of the endocardial pressure p^{endo} from the End Diastolic Pressure (EDP) p^{endo}_{EDP} (about 10 mmHg) to the one in the aorta p^{ao} (about 85 mmHg). We determine p^{endo} as the solution of

$$\frac{\mathrm{d}V^{endo}}{\mathrm{d}t}(p^{endo}) = 0, \qquad t \in (0, T_1], \tag{5}$$

where $V^{endo}(0)$ is set to the initial LV volume. Thus, we require that the ventricular volume V^{endo} remains constant; $T_1 = T_1(p^{endo})$ is the earliest time occurrence at which $p^{endo} \geq p^{ao}$;

2) Ejection: the ventricular volume V^{endo} decreases due to the contraction of the LV forcing the blood to flow through the aortic valve. We use a two elements Windkessel 0D model [83] in the form:

$$C\frac{\mathrm{d}p^{endo}}{\mathrm{d}t} = -\frac{p^{endo}}{R} - \frac{\mathrm{d}V^{endo}}{\mathrm{d}t}, \qquad t \in (T_1, T_2], \tag{6}$$

with $p^{endo}(T_1) = p^{ao}$ where represent the capacitance and resistance of the electric analog circuit mimicking the blood flow in the aorta. This phase ends when p^{endo} become smaller than p^{ao}, thus closing the aortic valve. Since we do not model the aortic pressure over time, we set in Eq. (6) $T_2 = T_2(V^{endo})$ as soon as $\frac{\mathrm{d}V^{endo}}{\mathrm{d}t}(T_2) \geq 0$;

3) Isovolumic relaxation: the endocardial pressure p^{endo} decreases as a consequence of the LV early relaxation while V^{endo} remains constant and is treated similarly to the isovolumic contraction (Eq. (5)). We denote the end time of this phase as $T_3 = T_3(p^{endo})$, the occurrence at which $p^{endo} \leq p^{endo}_{min}$ (about 5 mmHg);

4) Filling: the pressure drop in the LV causes the opening of the mitral valve, which in turn causes an increment of V^{endo} due to the blood flowing into the LV, until both the pressure p^{endo} and the volume V^{endo} reach the EDP values. We model this phase by linearly increasing p^{endo} until it reachs the value p^{endo}_{EDP} at the time $\overline{T}_3 = 0.7$ s, and we keep it constant from $\overline{T}_3$ to the final time $T = 0.8$ s, that is:

$$\frac{\mathrm{d}p^{endo}}{\mathrm{d}t} = \varsigma, \qquad t \in (T_3, T], \tag{7}$$

with $\varsigma = \frac{p^{endo}_{EDP} - p^{endo}(T_3)}{\overline{T}_3 - T_3}$ if $t \in (T_3, \overline{T}_3]$ and $\varsigma = 0$ if $t \in (\overline{T}_3 T]$.

3 Space and time discretizations

We briefly carry on the numerical discretization of the single core models (1), (2), and (3) with respect to the space and the time independent variables.

3.1 Space discretization

We use the Finite Element Method, FEM [62], for the space discretization of the PDEs of Section 2, thus obtaining a system of ODEs for each core model. We consider a mesh composed of pairwise disjoint tetrahedra $\mathcal{T}_h$ such that $\cup_{K \in \mathcal{T}_h} K = \Omega_0$, where h is the maximum size of the elements $K \in \mathcal{T}_h$. Then, we define the finite dimensional spaces $\mathcal{X}_h^r = \left\{ v \in C^0(\overline{\Omega}_0) \ : \ v|_K \in \mathbb{P}^r(K) \ \forall K \in \mathcal{T}_h \right\}$ and $\boldsymbol{\mathcal{X}}_h^r = [\mathcal{X}_h^r]^3$, where $\mathbb{P}^r(K)$ is the set of polynomials of degree smaller than or equal to r in the element K. By indicating with $\{\psi_j\}_{j=1}^{N_r^{\mathrm{dof}}}$ a basis for $\mathcal{X}_h^r$, it holds $\mathcal{X}_h^r = \mathrm{span}(\psi_1, \ldots, \psi_{N_r^{\mathrm{dof}}})$, $\boldsymbol{\mathcal{X}}_h^r = \mathrm{span}(\{\boldsymbol{\psi}_1^k\}_{k=1}^3, \ldots, \{\boldsymbol{\psi}_{N_r^{\mathrm{dof}}}^k\}_{k=1}^3)$, and $\boldsymbol{\psi}_j^k = \psi_j \mathbf{e}_k$, where $\mathbf{e}_k$ is the k-th unit vector of $\mathbb{R}^3$. We then denote by $\{\mathbf{x}_j\}_{j=1}^{N_r^{\mathrm{dof}}}$ the set of the Degrees of Freedom (DoFs) associated to $\mathcal{X}_h^r$ and $\boldsymbol{\mathcal{X}}_h^r$. The functions v_h, $\gamma_{f,h}$, and $\mathbf{d}_h$ are the FEM approximations of v, γ_f, and $\mathbf{d}$, respectively, and we denote by $\overline{\mathbf{v}}$, $\overline{\boldsymbol{\gamma}}_f$, and $\overline{\mathbf{d}}$ the vectors containing the nodal values of the primitive variables. Specifically, for the ionic variables $w_h^q(t) = \sum_{j=1}^{N_r^{\mathrm{dof}}} w_j^q(t)\psi_j$, where $w_j^q(t) \approx w_q(\mathbf{x}_j, t)$, from which $\overline{\mathbf{w}}^q(t) = \left\{ w_j^q(t) \right\}_{j=1}^{N_r^{\mathrm{dof}}}$ and $\overline{\mathbf{w}}(t) = \{\overline{\mathbf{w}}^q(t)\}_{q=1}^{N_I}$. Similarly, for the transmembrane potential

$v_h(t) = \sum_{j=1}^{N_r^{\text{dof}}} v_j(t)\psi_j$, where $v_j(t) \approx v(\mathbf{x}_j, t)$ and $\overline{\mathbf{v}}(t) = \{v_j(t)\}_{j=1}^{N_r^{\text{dof}}}$. For the active strain, $\gamma_{f,h}(t) = \sum_{j=1}^{N_r^{\text{dof}}} \gamma_{f,j}(t)\psi_j$, where $\gamma_{f,j}(t) \approx \gamma_f(\mathbf{x}_j, t)$ and $\overline{\boldsymbol{\gamma}}_f(t) = \{\gamma_{f,j}(t)\}_{j=1}^{N_r^{\text{dof}}}$. For the displacement, $\mathbf{d}_h(t) = \sum_{j=1}^{N_r^{\text{dof}}} \sum_{k=1}^{3} d_j^k(t)\boldsymbol{\psi}_j^k$, where $d_j^k(t) \approx \mathbf{d}(\mathbf{x}_j, t) \cdot \mathbf{e}_k$ and $\overline{\mathbf{d}}(t) = \left\{ \left\{ d_j^k(t) \right\}_{j=1}^{N_r^{\text{dof}}} \right\}_{k=1}^{3}$.

We write the equations of the ionic model at each node $\mathbf{x}_j$, $j = 1, \dots, N^{\text{dof}_r}$. The semi-discrete formulation of the ionic model hence reads: given $\overline{\mathbf{v}}(t)$, find $\overline{\mathbf{w}}(t)$ such that

$$\begin{cases} \dot{\overline{\mathbf{w}}}(t) + \mathbb{U}(\overline{\mathbf{v}}(t))\overline{\mathbf{w}}(t) = \mathbf{Q}(\overline{\mathbf{v}}(t)), \qquad t \in (0, T], \\ \overline{\mathbf{w}}(0) = \overline{\mathbf{w}}_0, \end{cases} \tag{8}$$

where $\mathbb{U}_{ii}(\overline{\mathbf{v}}) = \alpha_q(v_j) - \beta_q(v_j)$ and $\mathbf{Q}_i(\overline{\mathbf{v}}) = \alpha_q(v_j) w_q^{\infty}(v_j)$, with $i = q\, N_r^{\text{dof}} + j$, for $q = 1, \dots, N_I$, $j = 1, \dots, N_r^{\text{dof}}$.

For the monodomain equation we obtain instead the following semi-discrete problem: given $\overline{\mathbf{w}}(t)$ and $\overline{\mathbf{d}}(t)$, find $\overline{\mathbf{v}}(t)$ such that

$$\begin{cases} \mathbb{M}\dot{\overline{\mathbf{v}}}(t) + \mathbb{K}(\overline{\mathbf{d}}(t))\overline{\mathbf{v}}(t) + \mathbf{I}^{ion}(\overline{\mathbf{v}}(t), \overline{\mathbf{w}}(t)) = \mathbb{M}\mathbf{I}^{app}(t), \quad t \in (0, T], \\ \overline{\mathbf{v}}(0) = \overline{\mathbf{v}}_0, \end{cases} \tag{9}$$

where $\mathbb{M}_{ij} = \int_{\Omega_0} \psi_j \psi_i \, d\Omega_0$, $\mathbb{K}_{ij}(\overline{\mathbf{d}}_h) = \int_{\Omega_0} (J_h \mathbf{F}_h^{-1} \mathbf{D}_m \mathbf{F}_h^{-T} \nabla \psi_j) \cdot \nabla \psi_i \, d\Omega_0$, $\mathbf{I}_i^{ion}(\overline{\mathbf{v}}, \overline{\mathbf{w}}) = \int_{\Omega_0} I^{ion} \left(v_h, w_h^1, \dots, w_h^{N_I} \right) \psi_i \, d\Omega_0$, and $\mathbf{I}_i^{app}(t) = I^{app}(\mathbf{x}_i, t)$ for $i, j = 1, \dots, N_r^{\text{dof}}$ and $\overline{\mathbf{v}}_0 = \{v_0(\mathbf{x}_j)\}_{j=1}^{N_r^{\text{dof}}}$; $\mathbf{F}_h = \frac{\partial \mathbf{d}_h}{\partial \mathbf{X}}$ and $J_h = \det(\mathbf{F}_h)$. To overcome numerical instabilities [9], we use however a lumped mass matrix $\mathbb{M}^L$ in place of $\mathbb{M}$.

The semi-discrete formulation of the mechanical activation problem (2) reads: given $\overline{\mathbf{w}}(t)$ and $\overline{\mathbf{d}}(t)$, find $\overline{\boldsymbol{\gamma}}_f(t)$ such that

$$\begin{cases} \mathbb{M}\dot{\overline{\boldsymbol{\gamma}}}_f(t) + \varepsilon \mathbb{K}(\overline{\mathbf{w}}(t))\overline{\boldsymbol{\gamma}}_f(t) + \mathbf{\Phi}(\overline{\mathbf{w}}(t), \overline{\boldsymbol{\gamma}}_f(t), \overline{\mathbf{d}}(t)) = \mathbf{0} \quad t \in (0, T], \\ \overline{\boldsymbol{\gamma}}_f(0) = \mathbf{0}, \end{cases} \tag{10}$$

where $\mathbb{K}_{ij}(\overline{\mathbf{w}}) = \int_{\Omega_0} \frac{\varepsilon}{g(w_h^3)} \nabla \psi_j \cdot \nabla \psi_i \, d\Omega_0$ and $\mathbf{\Phi}_i(\overline{\mathbf{w}}, \overline{\boldsymbol{\gamma}}_f, \overline{\mathbf{d}}) = -\int_{\Omega_0} \frac{1}{g(w_h^3)} \Phi \left(w_h^3, \gamma_{f,h}, \mathbf{d}_h \right) \psi_i \, d\Omega_0$. for $i, j = 1, \dots, N_r^{\text{dof}}$.

The semi-discrete formulation of the mechanics problem (3) reads: given $\overline{\boldsymbol{\gamma}}_f(t)$, find $\overline{\mathbf{d}}(t)$ such that

$$\begin{cases} \rho_s \mathbb{M}_3 \ddot{\overline{\mathbf{d}}}(t) + \mathbb{F}\dot{\overline{\mathbf{d}}}(t) + \mathbb{G}\overline{\mathbf{d}}(t) + \mathbf{S}(\overline{\mathbf{d}}(t), \overline{\boldsymbol{\gamma}}_f(t)) = \mathbf{p}^{endo}(t) - \mathbf{S}_0, \quad t \in (0, T], \\ \overline{\mathbf{d}}(0) = \overline{\mathbf{d}}_0, \quad \dot{\overline{\mathbf{d}}}(0) = \mathbf{0}, \end{cases} \tag{11}$$

where $\mathbf{d}_0 = \left\{ \{\mathbf{d}_0(\mathbf{x}_j) \cdot \mathbf{e}_k\}_{j=1}^{N_r^{\mathrm{dof}}} \right\}_{k=1}^{3}$, $\mathbb{M}_3 = \mathrm{diag}\{\mathbb{M}, \mathbb{M}, \mathbb{M}\}$, $\mathbf{p}_i^{endo} = \int_{\Gamma_0^{endo}} p^{endo} \mathbf{N} \cdot \boldsymbol{\psi}_i$, $\mathbf{S}_{0,i} = \int_{\Omega_0} \mathbf{P}_0 : \nabla_0 \boldsymbol{\psi}_i^k \, d\Omega_0$, $\mathbb{F}_{ij}^k = \sum_{\eta \in \{epi,base\}} \int_{\Gamma_0^\eta} \left(C_\perp^\eta (\mathbf{N} \otimes \mathbf{N}) + C_\parallel^\eta (\mathbf{I} - \mathbf{N} \otimes \mathbf{N}) \right) \boldsymbol{\psi}_j^k \cdot \boldsymbol{\psi}_i^k \, d\Gamma_0$, $\mathbb{F} = \mathrm{diag}\left\{\mathbb{F}^k\right\}_{k=1}^3$, $\mathbb{G}_{ij}^k = \sum_{\eta \in \{epi,base\}} \int_{\Gamma_0^\eta} \left(K_\perp^\eta (\mathbf{N} \otimes \mathbf{N}) + K_\parallel^\eta (\mathbf{I} - \mathbf{N} \otimes \mathbf{N}) \right) \boldsymbol{\psi}_j^k \cdot \boldsymbol{\psi}_i^k \, d\Gamma_0$, $\mathbb{G} = \mathrm{diag}\left\{\mathbb{G}^k\right\}_{k=1}^3$, $\mathbf{S}_i^k(\overline{\mathbf{d}}, \overline{\boldsymbol{\gamma}}_f) = \int_{\Omega_0} \mathbf{P}(\mathbf{d}_h, \gamma_{f,h}) : \nabla_0 \boldsymbol{\psi}_i^k \, d\Omega_0$, $\mathbf{S}(\overline{\mathbf{d}}, \overline{\boldsymbol{\gamma}}_f) = \mathrm{diag}\left\{\mathbf{S}^k(\overline{\mathbf{d}}, \overline{\boldsymbol{\gamma}}_f)\right\}_{k=1}^3$ for $i, j = 1, \ldots, N_r^{\mathrm{dof}}$. The discretized prestress problem (4) can be similarly written as: find $(\widehat{\overline{\mathbf{d}}}_0, \overline{\mathbf{P}}_0)$ such that

$$\mathbb{G}\widehat{\overline{\mathbf{d}}}_0 + \mathbf{S}(\widehat{\overline{\mathbf{d}}}_{0,h}) = \overline{\mathbf{p}}_{EDP}^{endo} - \mathbf{S}_0. \tag{12}$$

3.2 Time discretization

We now carry on the time discretization for each of the semi-discrete single core problems of Section 3.1. For the electrophysiology several approaches have been proposed and used to solve the monodomain equation, in combination with the ionic model: explicit schemes [36, 67], implicit schemes [49, 59, 84], and implicit-explicit (IMEX) schemes [16, 74]. Regarding the mechanics, we consider an implicit scheme, while we consider both implicit and semi-implicit schemes for the electrophysiology. We symbolically rewrite the semi-discrete problems of Section 2 in the general form:

$$\begin{cases} \mathcal{M}_i \mathbf{z}_i(t) + \mathbf{T}_i(\mathbf{z}(t)) = \mathbf{H}_i(t) \quad t \in (0, T], & i = 1, \ldots, 4, \\ \mathbf{z}_i(0) = \mathbf{z}_{i,0}, & i = 1, \ldots, 4, \\ \dot{\mathbf{z}}_4(0) = \mathbf{0}, \end{cases} \tag{13}$$

where $\mathbf{z}_1 = \overline{\mathbf{w}}$, $\mathbf{z}_2 = \overline{\mathbf{v}}$, $\mathbf{z}_3 = \overline{\boldsymbol{\gamma}}_f$, $\mathbf{z}_4 = \overline{\mathbf{d}}$, and $\mathcal{M}_1 = \mathbb{I}\frac{\mathrm{d}}{\mathrm{dt}}$, $\mathcal{M}_2 = \mathcal{M}_3 = \mathbb{M}\frac{\mathrm{d}}{\mathrm{dt}}$, $\mathcal{M}_4 = \rho_s \mathbb{M}_3 \frac{\mathrm{d}^2}{\mathrm{dt}^2}$. The nonlinear vector-valued functions $\mathbf{T}_i$ and $\mathbf{H}_i$ are specific of the corresponding core model. In order to obtain a fully discretized formulation using the BDF scheme, we exploit the following approximation of the time derivatives:

$$\begin{aligned} \frac{\mathrm{d}}{\mathrm{dt}}\mathbf{z}_i(t^{n+1}) &\approx \frac{1}{\Delta t}\left(\vartheta_0^{\mathrm{I}} \mathbf{z}_i^{n+1} - \mathbf{z}_i^{\mathrm{I}}\right), & \mathbf{z}_i^{\mathrm{I}} &= \sum_{k=1}^{\sigma} \vartheta_k' \mathbf{z}_i^{n-k+1}, \qquad i = 1, \ldots, 4 \\ \frac{\mathrm{d}^2}{\mathrm{dt}^2}\mathbf{z}_4(t^{n+1}) &\approx \frac{1}{(\Delta t)^2}\left(\vartheta_0^{\mathrm{II}} \mathbf{z}_4^{n+1} - \mathbf{z}_4^{\mathrm{II}}\right), & \mathbf{z}_4^{\mathrm{II}} &= \sum_{k=1}^{\sigma+1} \vartheta_k^{\mathrm{II}} \mathbf{z}_4^{n-k+1}, \end{aligned} \tag{14}$$

where $\Delta t = \frac{T}{N_T}$ is the timestep size, N_T being the number of subintervals, while the parameters $\vartheta_k', \vartheta_k'', k = 0, \ldots, \sigma$ depend on the order σ of the BDF scheme.

In the implicit case, we obtain the following nonlinear systems:

$$\mathbf{A}_i(\mathbf{z}^{n+1}) = \mathbf{b}_i^{n+1}, \qquad i = 1, \ldots, 4, \quad n = \sigma, \ldots, N_T - 1, \tag{15}$$

with $\mathbf{z}^n$ assigned for $n = 0, \dots, \sigma$. In the semi-implicit case, on the other hand, we extrapolate the variables in the nonlinear terms $\mathbf{A}_i(\mathbf{z}^{n+1})$ by means of the Newton-Gregory backward polynomials [11] – as done, e.g., for the Navier-Stokes equations in [29] – thus yielding a linear system at each timestep. The extrapolated variables are evaluated by means of an approximation of the same order σ of the BDF scheme as $\mathbf{z}_i(t^{n+1}) \approx \mathbf{z}_i^* = \sum_{k=1}^{\sigma} \beta_k \mathbf{z}_i^{n-k+1}$. We thus approximate the nonlinear terms as $\mathbf{A}_i(\mathbf{z}^{n+1}) \approx \sum_{j=1}^{4} \mathbb{A}_{i,j}(\mathbf{z}^*)\mathbf{z}_j^{n+1} + \widetilde{\mathbf{A}}_i(\mathbf{z}^*)$, with notation being understood. By recalling Eq. (15), we hence obtain a system in the form:

$$\sum_{j=1}^{4} \mathbb{A}_{i,j}(\mathbf{z}^*)\mathbf{z}_j^{n+1} = \mathbf{b}_i^{n+1} \qquad n = \sigma, \dots, N_T - 1, \tag{16}$$

with $\mathbf{z}^n$ assigned for $n = 0, \dots, \sigma$ and $\mathbf{b}_i^{n+1} = \mathbf{h}_i^{n+1} - \widetilde{\mathbf{A}}_i(\mathbf{z}^*)$.

3.2.1 Discretization of the 0D fluid model

We evaluate the volume $V^{endo}(t)$ at time t^n by exploiting the formula reported in [67]. For the discretization of the 0D fluid models of Section 2.4 in terms of p^{endo}, we consider the following approaches tailored on the phase of the heartbeat (we drop the "*endo*" superscript for simplicity). At each n:

1) Isovolumic contraction: we use an inexact Newton method to solve Eq. (5) by iteratively updating the pressure as $p_{k+1}^{n+1} = p_k^{n+1} - \frac{\Delta t}{\zeta}(V_k^{n+1} - V^n)$, for $k = 0, 1, \dots$ with $p_0^{n+1} = p^n$ and $V_0^{n+1} = V^n$. By dimensional arguments, we approximate $\frac{\partial V}{\partial p}(p_k^{n+1})$ as $-\frac{\Delta t}{\zeta}\left[\frac{mm^4 s^2}{g}\right]$ in the Newton iterate. At each iteration, p_{k+1}^{n+1} is used to solve the electromechanics problem thus obtaining V_{k+1}^{n+1}; the procedure is repeated until the condition $\frac{|V_{k+1}^{n+1} - V^n|}{\Delta t} < \varepsilon$ is satisfied. The parameter $\zeta < 0$ has to be "sufficiently" small in order for the fixed point algorithm to converge;

2) Ejection: the two elements Windkessel model (6) is solved in the pressure variable with a BDF scheme of order $\sigma = 1$:

$$C\frac{p^{n+1} - p^n}{\Delta t} = -\frac{p^{n+1}}{R} - \frac{V^n - V^{n-1}}{\Delta t}; \tag{17}$$

3) Isovolumic relaxation: we proceed as in 1);

4) Filling: the pressure is simply updated as $p^{n+1} = p^n + \Delta t \, \varsigma$.

4 Numerical coupling: segregated strategies

We now recall the monolithic strategy that we introduced in [28], and we propose three new segregated strategies for the solution of the electromechanics problem.

4.1 Fully monolithic strategy ($\mathcal{I}_\mathrm{I}\mathcal{E}_\mathrm{I}\mathcal{A}_\mathrm{I}\mathcal{M}_\mathrm{I}$)

We use the implicit scheme (15) for the time discretization of each core model and we assemble the integrated problem in a monolithic fashion, thus considering a "strong" coupling among the fully discretized core models; see [28]. This accounts to solve, for $n = \sigma, \dots, N_T - 1$, the following system of size $8 \times N_r^{\mathrm{dof}}$:

$$
(\mathcal{I}_\mathrm{I}\mathcal{E}_\mathrm{I}\mathcal{A}_\mathrm{I}\mathcal{M}_\mathrm{I}): \begin{cases}
\left(\dfrac{\vartheta_0^\mathrm{I}}{\Delta t} + \mathbb{U}(\overline{\mathbf{v}}^{n+1}) \right) \overline{\mathbf{w}}^{n+1} - \mathbf{Q}(\overline{\mathbf{v}}^{n+1}) = \dfrac{1}{\Delta t} \overline{\mathbf{w}}^\mathrm{I}, \\
\left(\dfrac{\vartheta_0^\mathrm{I}}{\Delta t} \mathbb{M} + \mathbb{K}(\overline{\mathbf{d}}^{n+1}) \right) \overline{\mathbf{v}}^{n+1} + \mathbf{I}^{ion}(\overline{\mathbf{v}}^{n+1}, \overline{\mathbf{w}}^{n+1}) = \dfrac{1}{\Delta t} \mathbb{M} \overline{\mathbf{v}}^\mathrm{I} + \mathbb{M} \mathbf{I}^{app}(t^{n+1}), \\
\left(\dfrac{\vartheta_0^\mathrm{I}}{\Delta t} \mathbb{M} + \varepsilon \mathbb{K}(\overline{\mathbf{w}}^{n+1}) \right) \overline{\boldsymbol{\gamma}}_f^{n+1} + \mathbf{\Phi}(\overline{\mathbf{w}}^{n+1}, \overline{\boldsymbol{\gamma}}_f^{n+1}, \overline{\mathbf{d}}^{n+1}) = \dfrac{1}{\Delta t} \mathbb{M} \overline{\boldsymbol{\gamma}}_f^\mathrm{I}, \\
\left(\rho_s \dfrac{\vartheta_0^\mathrm{II}}{(\Delta t)^2} \mathbb{M}_3 + \dfrac{\vartheta_0^\mathrm{I}}{\Delta t} \mathbb{F} + \mathbb{G} \right) \overline{\mathbf{d}}^{n+1} + \mathbf{S}(\overline{\mathbf{d}}^{n+1}, \overline{\boldsymbol{\gamma}}_f^{n+1}) \\
\qquad\qquad = \rho_s \dfrac{1}{(\Delta t)^2} \mathbb{M}_3 \overline{\mathbf{d}}^\mathrm{II} + \dfrac{1}{\Delta t} \mathbb{F} \overline{\mathbf{d}}^\mathrm{I} + \mathbf{p}^{endo}(t^{n+1}) - \mathbf{S}_0,
\end{cases} \tag{18}
$$

which we indicate as ($\mathcal{I}_\mathrm{I}\mathcal{E}_\mathrm{I}\mathcal{A}_\mathrm{I}\mathcal{M}_\mathrm{I}$), where the subscript I stands for the implicit solver, and compactly rewrite in algebraic form as

$$
\mathbf{A}_{EM}^{n+1}(\mathbf{z}^{n+1}) = \mathbf{b}_{EM}^{n+1}, \tag{19}
$$

with notation being understood. We then apply, at each timestep, the Newton method [62] to approximate the solution of the nonlinear problem (19) by iteratively solving the linear system

$$
\mathbb{J}_{EM,k}^{n+1} \delta \mathbf{z}_{k+1}^{n+1} = -\mathbf{r}_k^{n+1} \quad \text{with} \quad \mathbf{z}_{k+1}^{n+1} = \mathbf{z}_k^{n+1} + \delta \mathbf{z}_{k+1}^{n+1}, \tag{20}
$$

for $k = 0, \dots,$ until $\|\mathbf{r}_k^{n+1}\|_{L^2} < \varepsilon_{tol}^N$, where ε_{tol}^N is a given tolerance. $\mathbb{J}_{EM,k}^{n+1}$ is the Jacobian matrix of (19), evaluated in $\mathbf{z}_k^{n+1}$, and is endowed with the following block structure:

$$
\mathbb{J}_{EM} = \begin{bmatrix}
\boxed{\begin{matrix} J_{11} & J_{12} \\ J_{21} & J_{22} \end{matrix}} & \begin{matrix} 0 & 0 \\ 0 & J_{24} \end{matrix} \\
\begin{matrix} J_{31} & 0 \\ 0 & 0 \end{matrix} & \begin{matrix} \boxed{J_{33}} & J_{34} \\ J_{43} & \boxed{J_{44}} \end{matrix}
\end{bmatrix} \tag{21}
$$

while the residual is defined as $\mathbf{r}_k^{n+1} = \mathbf{b}_{EM}^{n+1} - \mathbf{A}_{EM}^{n+1}(\mathbf{z}_k^{n+1})$. In (21) we highlight the diagonal blocks corresponding to the electrophysiology, the mechanical activation, and the mechanics, respectively. We use the preconditioned GMRES method [71] to solve problem (20). We exploit a lower block triangular Gauss-Seidel right preconditioner $\mathcal{P}_{EM}$ introduced

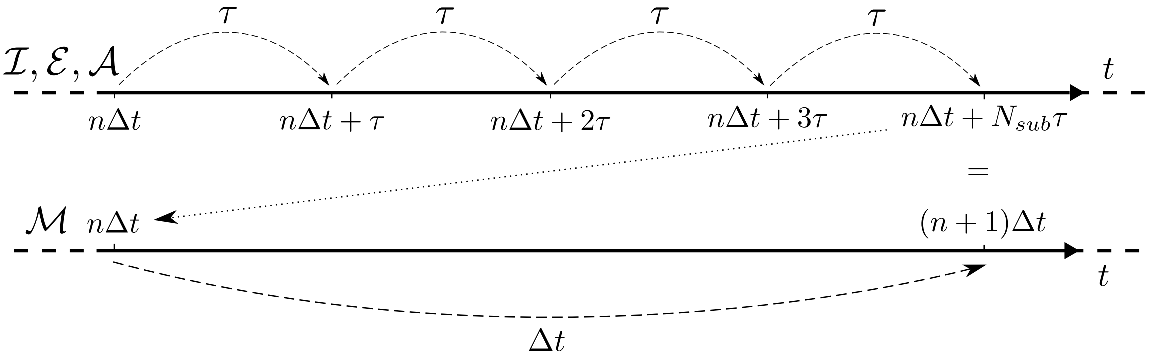

Figure 3: Graphical representation of the time advancement for $(\mathcal{I}_\mathrm{I}\mathcal{E}_\mathrm{I}\mathcal{A}_\mathrm{I})$–$(\mathcal{M}_\mathrm{I})$ and $(\mathcal{I}_\mathrm{SI}\mathcal{E}_\mathrm{SI}\mathcal{A}_\mathrm{SI})$–$(\mathcal{M}_\mathrm{I})$

in [28], a generalization of the FaCSI preconditioner of [23, 24, 27]. $\mathcal{P}_{EM}$ is obtained by dropping the upper triangular blocks of matrix $\mathbb{J}_{EM}$, namely J_{12}, J_{24}, and J_{34}, and then by substituting the diagonal blocks with black-box Algebraic Multigrid (AMG) and Additive Schwarz preconditioners. With this strategy, we are able to exploit the information of the core problems at the block level, that is we use a preconditioner that exploits the "physics" of the coupled problem.

While $(\mathcal{I}_\mathrm{I}\mathcal{E}_\mathrm{I}\mathcal{A}_\mathrm{I}\mathcal{M}_\mathrm{I})$ is "numerically" stable and convergent as long as the initial guess $\mathbf{z}_0^{n+1}$ in (20) is, at each time, "sufficiently" close to the solution, it also requires to use the same timestep for the time discretization of each core model. Hence, even if the electrophysiology and the mechanics are characterized by very different time scales, the former dictates our choice for the timestep of the fully monolithic problem.

4.2 Partially segregated strategy $(\mathcal{I}_\mathrm{I}\mathcal{E}_\mathrm{I}\mathcal{A}_\mathrm{I})$–$(\mathcal{M}_\mathrm{I})$

We break the strong coupling between the electrophysiology and the mechanical activation $(\mathcal{I}_\mathrm{I}\mathcal{E}_\mathrm{I}\mathcal{A}_\mathrm{I})$ and the tissue mechanics $(\mathcal{M}_\mathrm{I})$. We hence evaluate the terms $\mathbb{K}(\overline{\mathbf{d}}^{n+1})$ and $\mathbf{\Phi}(\overline{\mathbf{w}}^{n+1}, \overline{\gamma}_f^{n+1}, \overline{\mathbf{d}}^{n+1})$ of Eq. (18) in the extrapolated variable $\overline{\mathbf{d}}^{*}$ instead of $\overline{\mathbf{d}}^{n+1}$, thus obtaining two separated problems which are solved in a segregated fashion. This strategy is equivalent to the application of a (first order) Godunov splitting scheme [32] to the monolithic problem. We notice that the $(\mathcal{I}_\mathrm{I}\mathcal{E}_\mathrm{I}\mathcal{A}_\mathrm{I})$ problem is still fully coupled, while it is decoupled from the $(\mathcal{M}_\mathrm{I})$ block, hence the denomination $(\mathcal{I}_\mathrm{I}\mathcal{E}_\mathrm{I}\mathcal{A}_\mathrm{I})$–$(\mathcal{M}_\mathrm{I})$.

This approach allows to use a smaller timestep for the $(\mathcal{I}_\mathrm{I}\mathcal{E}_\mathrm{I}\mathcal{A}_\mathrm{I})$ problem, which we denote by τ, with respect to the one used for the mechanics $(\mathcal{M}_\mathrm{I})$: we set in particular

$$\tau = \frac{\Delta t}{N_{sub}},$$

where $N_{sub} \in \mathbb{N}$ is the number of intermediate substeps; τ is the timestep size of $(\mathcal{I}_\mathrm{I}\mathcal{E}_\mathrm{I}\mathcal{A}_\mathrm{I})$

and Δt that of $(\mathcal{M}_\mathrm{I})$. This implies that $\tau \leq \Delta t$ and $t^{n+\frac{m}{N_{sub}}} = t^n + m\tau$ for $m = 1, \dots, N_{sub}$. N_{sub} can also be regarded as the ratio of the timestep lengths used for the mechanics and for the electrophysiology and activation. The overall time advancement is represented in Figure 3. Another clear advantage of this approach is that, in the isovolumic phases, only the mechanics problem needs to be solved, contrarily to the fully monolithic one where Eq. (18) has to be solved at each subiteration. Problem $(\mathcal{I}_\mathrm{I}\mathcal{E}_\mathrm{I}\mathcal{A}_\mathrm{I})$ from t^n to t^{n+1} reads:

$$(\mathcal{I}_\mathrm{I}\mathcal{E}_\mathrm{I}\mathcal{A}_\mathrm{I}): \begin{cases} \left(\dfrac{\vartheta_0^\mathrm{I}}{\tau} + \mathbb{U}(\overline{\mathbf{v}}^{n+\frac{m}{N_{sub}}})\right)\overline{\mathbf{w}}^{n+\frac{m}{N_{sub}}} - \mathbf{Q}(\overline{\mathbf{v}}^{n+\frac{m}{N_{sub}}}) = \dfrac{1}{\tau}\overline{\mathbf{w}}^\mathrm{I}, \\ \left(\dfrac{\vartheta_0^\mathrm{I}}{\tau}\mathbb{M} + \mathbb{K}(\overline{\mathbf{d}}^*)\right)\overline{\mathbf{v}}^{n+\frac{m}{N_{sub}}} + \mathbf{I}^{ion}(\overline{\mathbf{v}}^{n+\frac{m}{N_{sub}}}, \overline{\mathbf{w}}^{n+\frac{m}{N_{sub}}}) = \dfrac{1}{\tau}\mathbb{M}\overline{\mathbf{v}}^\mathrm{I} + \mathbb{M}\mathbf{I}^{app}(t^{n+\frac{m}{N_{sub}}}), \\ \left(\dfrac{\vartheta_0^\mathrm{I}}{\tau}\mathbb{M} + \varepsilon\mathbb{K}(\overline{\mathbf{w}}^{n+\frac{m}{N_{sub}}})\right)\overline{\boldsymbol{\gamma}}_f^{n+\frac{m}{N_{sub}}} + \boldsymbol{\Phi}(\overline{\mathbf{w}}^{n+\frac{m}{N_{sub}}}, \overline{\boldsymbol{\gamma}}_f^{n+\frac{m}{N_{sub}}}, \overline{\mathbf{d}}^*) = \dfrac{1}{\tau}\mathbb{M}\overline{\boldsymbol{\gamma}}_f^\mathrm{I}, \end{cases} \tag{22}$$

for $m = 1, \dots, N_{sub}$, where the terms $\overline{\mathbf{w}}^\mathrm{I}$, $\overline{\mathbf{v}}^\mathrm{I}$, and $\overline{\boldsymbol{\gamma}}_f^\mathrm{I}$ (defined in Eq. (14)) are evaluated by using the variables at times $t^n, t^n - \tau, \dots, t^n - (\sigma - 1)\tau$. As in the case of the implicit electromechanics, we use the Newton method to solve problem (22), and the block structure of the correspondent Jacobian matrix $\mathbb{J}_\mathrm{EA}$ is:

$$\mathbb{J}_{EA} = \left[\begin{array}{ccc} \boxed{\begin{array}{cc} J_{11} & J_{12} \\ J_{21} & J_{22} \end{array}} & \begin{array}{c} 0 \\ 0 \end{array} \\ \begin{array}{cc} J_{31} & 0 \end{array} & \boxed{J_{33}.} \end{array}\right] \tag{23}$$

We exploit the same preconditioning technique that was outlined in Section 4.1 for the $(\mathcal{I}_\mathrm{I}\mathcal{E}_\mathrm{I}\mathcal{A}_\mathrm{I}\mathcal{M}_\mathrm{I})$ strategy, only restricted to the block $(\mathcal{I}_\mathrm{I}\mathcal{E}_\mathrm{I}\mathcal{A}_\mathrm{I})$. After solving Eq. (22) for N_{sub} steps, we solve at t^{n+1} the implicit mechanics problem $(\mathcal{M}_\mathrm{I})$:

$$(\mathcal{M}_\mathrm{I}): \quad \begin{aligned} &\left(\rho_s \frac{\vartheta_0^\mathrm{II}}{(\Delta t)^2}\mathbb{M}_3 + \frac{\vartheta_0'}{\Delta t}\mathbb{F} + \mathbb{G}\right)\overline{\mathbf{d}}^{n+1} + \mathbf{S}(\overline{\mathbf{d}}^{n+1}, \overline{\boldsymbol{\gamma}}_f^{n+1}) \\ &= \rho_s \frac{1}{(\Delta t)^2}\mathbb{M}_3\overline{\mathbf{d}}^\mathrm{II} + \frac{1}{\Delta t}\mathbb{F}\overline{\mathbf{d}}^\mathrm{I} + \mathbf{p}^{endo}(t^{n+1}) - \mathbf{S}_0, \end{aligned} \tag{24}$$

by means of the Newton method. We highlight that the vector $\overline{\boldsymbol{\gamma}}_f^{n+1}$ in Eq. (24) is already known, since it is given after the last step of Eq. (22) (i.e. for $m = N_{sub}$).

4.3 Partially segregated strategy $(\mathcal{I}_{\mathrm{SI}}\mathcal{E}_{\mathrm{SI}}\mathcal{A}_{\mathrm{SI}})$–$(\mathcal{M}_{\mathrm{I}})$

By considering now the semi-implicit scheme (subscript SI) for the time discretization, the $(\mathcal{I}_{\mathrm{SI}}\mathcal{E}_{\mathrm{SI}}\mathcal{A}_{\mathrm{SI}})$ problem reads:

$$(\mathcal{I}_{\mathrm{SI}}\mathcal{E}_{\mathrm{SI}}\mathcal{A}_{\mathrm{SI}}): \begin{cases} \left(\dfrac{\vartheta_0^{\mathrm{I}}}{\Delta t} + \mathbb{U}(\overline{\mathbf{v}}^*)\right)\overline{\mathbf{w}}^{n+\frac{m}{N_{sub}}} = \dfrac{1}{\tau}\overline{\mathbf{w}}^{\mathrm{I}} + \mathbf{Q}(\overline{\mathbf{v}}^*), \\ \left(\dfrac{\vartheta_0^{\mathrm{I}}}{\Delta t}\mathbb{M} + \mathbb{K}(\overline{\mathbf{d}}^*) + \mathbb{I}_v^{ion}(\overline{\mathbf{v}}^*, \overline{\mathbf{w}}^*)\right)\overline{\mathbf{v}}^{n+\frac{m}{N_{sub}}} + \mathbb{I}_{\mathbf{w}}^{ion}(\overline{\mathbf{v}}^*, \overline{\mathbf{w}}^*)\overline{\mathbf{w}}^{n+\frac{m}{N_{sub}}} \\ \qquad\qquad = \dfrac{1}{\tau}\mathbb{M}\overline{\mathbf{v}}^{\mathrm{I}} + \widetilde{\mathbf{I}}^{ion}(\overline{\mathbf{v}}^*, \overline{\mathbf{w}}^*) + \mathbb{M}\mathbf{I}^{app}(t^{n+\frac{m}{N_{sub}}}), \\ \left(\dfrac{\vartheta_0^{\mathrm{I}}}{\tau}\mathbb{M} + \varepsilon\mathbb{K}(\overline{\mathbf{w}}^*) + \mathbb{P}_{\gamma_f}(\overline{\mathbf{w}}^*, \overline{\boldsymbol{\gamma}}_f^*, \overline{\mathbf{d}}^*)\right)\overline{\boldsymbol{\gamma}}_f^{n+\frac{m}{N_{sub}}} = \dfrac{1}{\tau}\mathbb{M}\overline{\boldsymbol{\gamma}}_f^{\mathrm{I}} + \widetilde{\boldsymbol{\Phi}}(\overline{\mathbf{w}}^*, \overline{\boldsymbol{\gamma}}_f^*, \overline{\mathbf{d}}^*), \end{cases} \tag{25}$$

for $m = 1, \ldots, N_{sub}$. In this case, the block pattern of the matrix $\mathbb{A}_{EA}$, stemming from the linear system (25), is:

$$\mathbb{A}_{EA} = \left[\begin{array}{cc} \boxed{\begin{matrix} A_{11} & 0 \\ A_{21} & A_{22} \end{matrix}} & \begin{matrix} 0 \\ 0 \end{matrix} \\ \begin{matrix} 0 & 0 \end{matrix} & \boxed{A_{33}} \end{array}\right]. \tag{26}$$

As in the case of the $(\mathcal{I}_{\mathrm{I}}\mathcal{E}_{\mathrm{I}}\mathcal{A}_{\mathrm{I}})$ strategy, after solving Eq. (25) for N_{sub} steps, we solve the implicit mechanics problem $(\mathcal{M}_{\mathrm{I}})$ (24).

4.4 Fully segregated strategy $(\mathcal{I}_{\mathrm{SI}})$–$(\mathcal{E}_{\mathrm{SI}})$–$(\mathcal{A}_{\mathrm{SI}})$–$(\mathcal{M}_{\mathrm{I}})$

Finally, we further segregate the $(\mathcal{I}_{\mathrm{SI}}\mathcal{E}_{\mathrm{SI}}\mathcal{A}_{\mathrm{SI}})$ block, that is instead of solving $(\mathcal{I}_{\mathrm{SI}}\mathcal{E}_{\mathrm{SI}}\mathcal{A}_{\mathrm{SI}})$ (25) in a monolithic fashion, we solve the three subproblems sequentially. In Figure 4 we show a representation of the time advancement in this case. At each time t^n, the algorithm amounts to perform, for $m = 1, \ldots, N_{sub}$, the following steps, in order:

1. find $\overline{\mathbf{w}}^{n+\frac{m}{N_{sub}}}$ by solving:

$$(\mathcal{I}_{\mathrm{SI}}): \qquad \left(\frac{\vartheta_0^{\mathrm{I}}}{\Delta t} + \mathbb{U}(\overline{\mathbf{v}}^*)\right)\overline{\mathbf{w}}^{n+\frac{m}{N_{sub}}} = \frac{1}{\tau}\overline{\mathbf{w}}^{\mathrm{I}} + \mathbf{Q}(\overline{\mathbf{v}}^*); \tag{27}$$

2. use $\overline{\mathbf{w}}^{n+\frac{m}{N_{sub}}}$, obtained with Eq. (27), to find $\overline{\mathbf{v}}^{n+\frac{m}{N_{sub}}}$ by solving:

$$(\mathcal{E}_{\mathrm{SI}}): \quad \begin{aligned} &\left(\frac{\vartheta_0^{\mathrm{I}}}{\Delta t}\mathbb{M} + \mathbb{K}(\overline{\mathbf{d}}^*) + \mathbb{I}_v^{ion}(\overline{\mathbf{v}}^*, \overline{\mathbf{w}}^{n+\frac{m}{N_{sub}}})\right)\overline{\mathbf{v}}^{n+\frac{m}{N_{sub}}} \\ &= \frac{1}{\tau}\mathbb{M}\overline{\mathbf{v}}^{\mathrm{I}} + \widetilde{\mathbf{I}}^{ion}(\overline{\mathbf{v}}^*, \overline{\mathbf{w}}^{n+\frac{m}{N_{sub}}}) - \mathbb{I}_{\mathbf{w}}^{ion}(\overline{\mathbf{v}}^*, \overline{\mathbf{w}}^{n+\frac{m}{N_{sub}}})\overline{\mathbf{w}}^{n+\frac{m}{N_{sub}}} + \mathbb{M}\mathbf{I}^{app}(t^{n+\frac{m}{N_{sub}}}); \end{aligned} \tag{28}$$

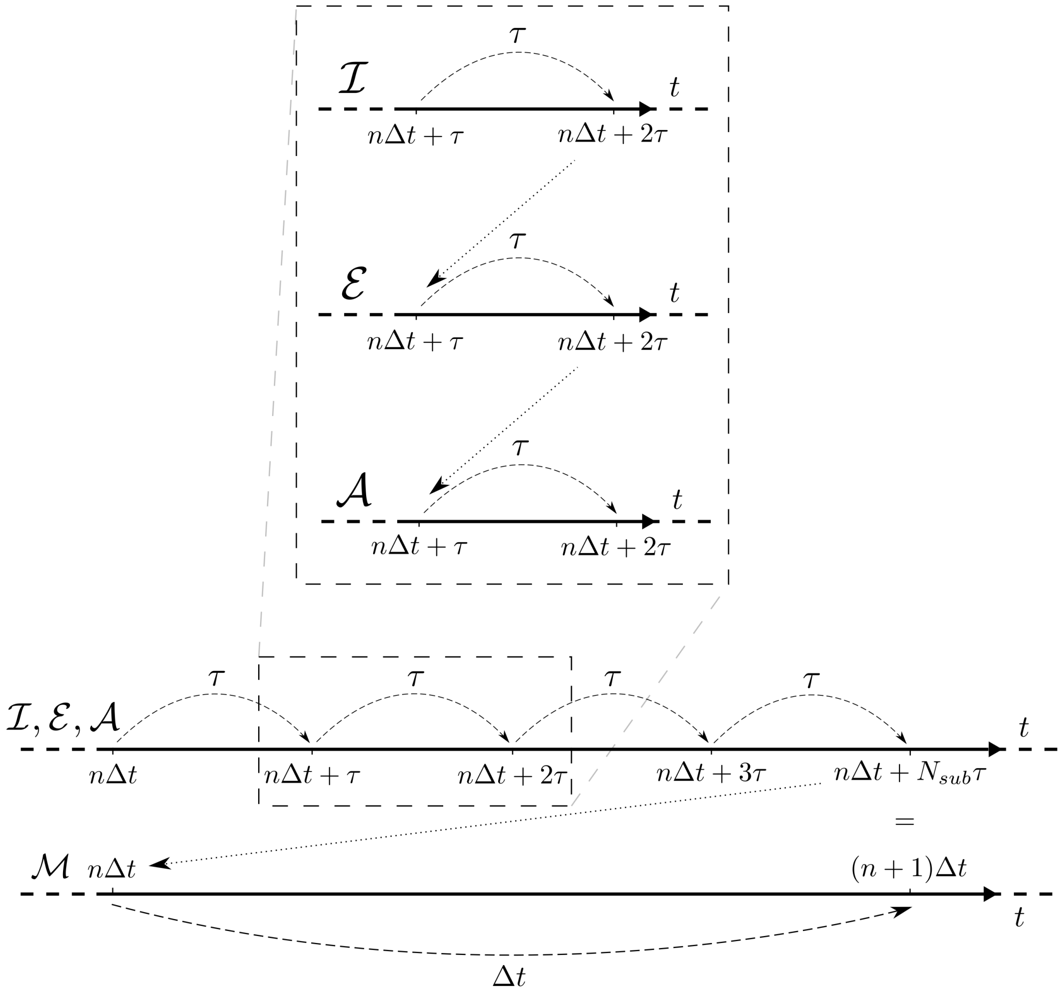

Figure 4: Graphical representation of the time advancement for $(\mathcal{I}_{\mathrm{SI}})$–$(\mathcal{E}_{\mathrm{SI}})$–$(\mathcal{A}_{\mathrm{SI}})$–$(\mathcal{M}_{\mathrm{I}})$

3. use $\overline{\mathbf{w}}^{n+\frac{m}{N_{sub}}}$ and $\overline{\mathbf{v}}^{n+\frac{m}{N_{sub}}}$, obtained with Eq. (27) and Eq. (28), to find $\overline{\boldsymbol{\gamma}}_f^{n+\frac{m}{N_{sub}}}$ by solving:

$$(\mathcal{A}_{\mathrm{SI}}): \qquad \begin{aligned} &\left(\frac{\vartheta_0^{\mathrm{I}}}{\tau}\mathbb{M} + \varepsilon\mathbb{K}(\overline{\mathbf{w}}^{n+\frac{m}{N_{sub}}}) + \mathbb{P}^{\gamma_f}(\overline{\mathbf{w}}^{n+\frac{m}{N_{sub}}}, \overline{\boldsymbol{\gamma}}_f^*, \overline{\mathbf{d}}^*)\right)\overline{\boldsymbol{\gamma}}_f^{n+\frac{m}{N_{sub}}} \\ &\qquad = \frac{1}{\tau}\mathbb{M}\overline{\boldsymbol{\gamma}}_f^{\mathrm{I}} + \widetilde{\boldsymbol{\Phi}}(\overline{\mathbf{w}}^{n+\frac{m}{N_{sub}}}, \overline{\boldsymbol{\gamma}}_f^*, \overline{\mathbf{d}}^*). \end{aligned} \tag{29}$$

After N_{sub} steps, we once again solve problem (24) and finally obtain $\overline{\mathbf{d}}^{n+1}$.

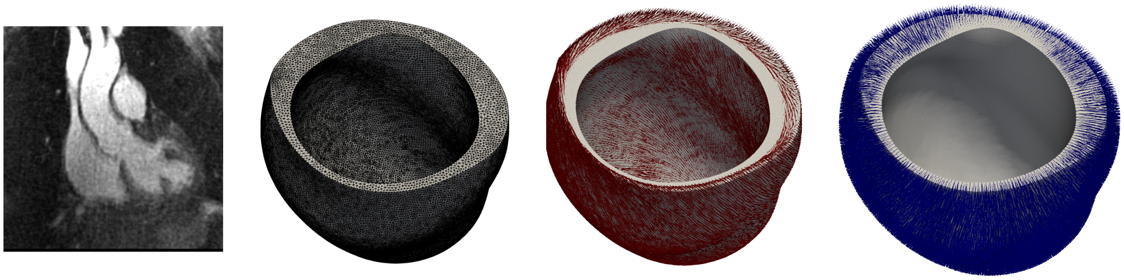

Figure 5: From left to right: the MRI from which the subject-specific geometry was segmented, the mesh, the fibers field, and the sheets field.

5 Numerical results

In this section we first briefly describe the procedures used to obtain the geometries, the fibers and the sheets fields, and the prestress, then we test the three segregated schemes on benchmark problems in idealized and subject-specific LV geometries. The idealized mesh features 1'827 vertices and 6'500 tetrahedra, while the subject-specific mesh features 126'031 vertices and 637'379 tetrahedra. We use finite elements of order $r = 1$ and BDF of order $\sigma = 1$ (i.e. Backward Euler) and $\sigma = 2$ for the time discretization to ensure A-stability [62].

For all the simulations we use LifeV[1], an open-source finite element library for the solution of problems described by PDEs in a High Performance Computing framework.

5.1 Preprocessing

Image segmentation locates regions of interest (ROI) in the form of a subset of pixels [35], and amounts to assign different flags to regions containing different types of tissues and/or fluids. In this work, to obtain the subject-specific mesh, we used a manual procedure exploiting the brightness of the pixels of a 3D MRI image[2]; see Figure 5.

Fibers and sheets field distributions in the myocardium are not tipically extracted from MRIs, unless special procedures are applied [64]. For this reason, several mathematically rule-based definition of these fields have been used [33, 45, 50, 69], which attempt to construct their orientation. At the epicardium and at the endocardium, the fiber direction $\mathbf{f}_0$ is tangential to the boundary, while the sheet direction $\mathbf{s}_0$ belongs to the plane identified by the normal and the ventricle centerline (i.e. the line passing through the center of the ventricle). In the most general case, angles α_{endo}, α_{epi}, β_{endo}, and β_{epi}, representing

---

[1] https://cmcsforge.epfl.ch

[2] The MRI images are provided by Prof. J. Schwitter (Chief physician at the Centre Hospitalier Universitaire Vaudois CHUV, Lausanne) and Dr. P. Masci (CHUV) in the framework of the collaboration CMCS@EPFL–CHUV.

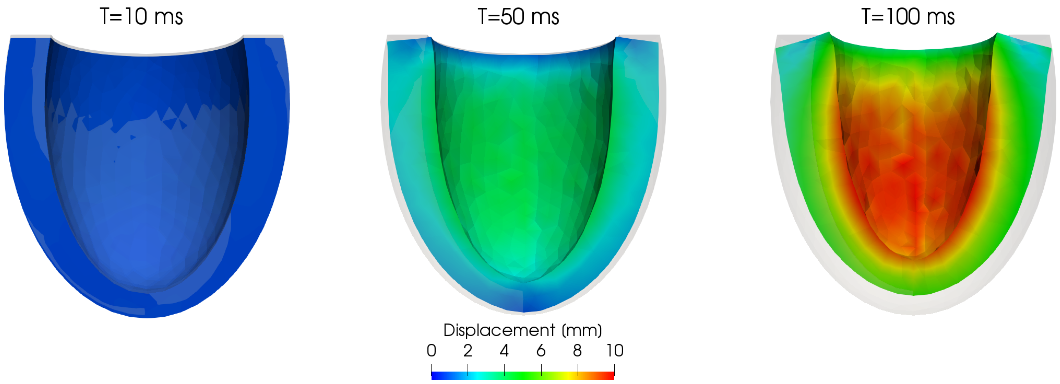

Figure 6: Idealized LV and magnitude of the displacement field at different times, compared with the reference domain Ω_0, for the benchmark problem.

the inclination of the fibers and the sheets with respect to the base plane, are assigned. The direction of fibers and sheets inside the myocardium is determined by a transmurally linear mapping. Here we consider the rule-based algorithm proposed in [86] and further developed in [67]; we set $\alpha_{endo} = -60°$, $\alpha_{epi} = +60°$, $\beta_{endo} = \beta_{epi} = 0°$. In Figure 5, we show the fields obtained by applying the algorithm to the subject-specific mesh.

Regarding the prestress, we solve problem (12) by means of a continuation method. More precisely, given the EDP value p_{EDP}^{endo} and an integer S representing the number of steps, we first define a pressure ramp increment in the form: $p_k = \frac{k}{S} p_{EDP}^{endo}, \quad k = 1, \ldots, S$. For each $k = 1, \ldots, S$, we set $p = p_k$ in Eq. (4) and solve the nonlinear system (in $\mathbf{d}$) by using the Newton method to obtain an increasingly accurate approximation of $\mathbf{P}_{0,k}$, i.e. the prestress corresponding to the pressure p_k. We refer the reader to [28] for more details.

5.2 Benchmark problem with idealized geometry

In order to assess the properties of the proposed segregated schemes and to evaluate their behavior for different timestep sizes, we set up and solve a benchmark problem by using the idealized geometry. The contraction is triggered by applying a current in three distinct points at the endocardium while keeping the pressure at the EDP value $p_{EDP}^{endo} = 10$ mmHg. We choose this setting so that the volume of the idealized LV halves during the simulation, from the initial value of approximately 136 ml to around 68 ml, thus attaining a deformation which is comparable with physiological data. We set $T = 0.1$ s and $\tau = 1, 2, 4, 8, 12, 16, 24, 32 \times 10^{-5}$ s, with $N_{sub} = 1, 2, 4, 8, 16$ for the segregated strategies (being $\Delta t = N_{sub}\tau$ the timestep size for the mechanics), while $\Delta t = \tau$ for the monolithic strategy. The absolute tolerances for the Newton method and the GMRES solver are set to $\varepsilon_{tol}^{N} = 10^{-4}$ and $\varepsilon_{tol}^{G} = 10^{-8}$, respectively. For all the numerical simulations of this benchmark, 6 cpus are used.

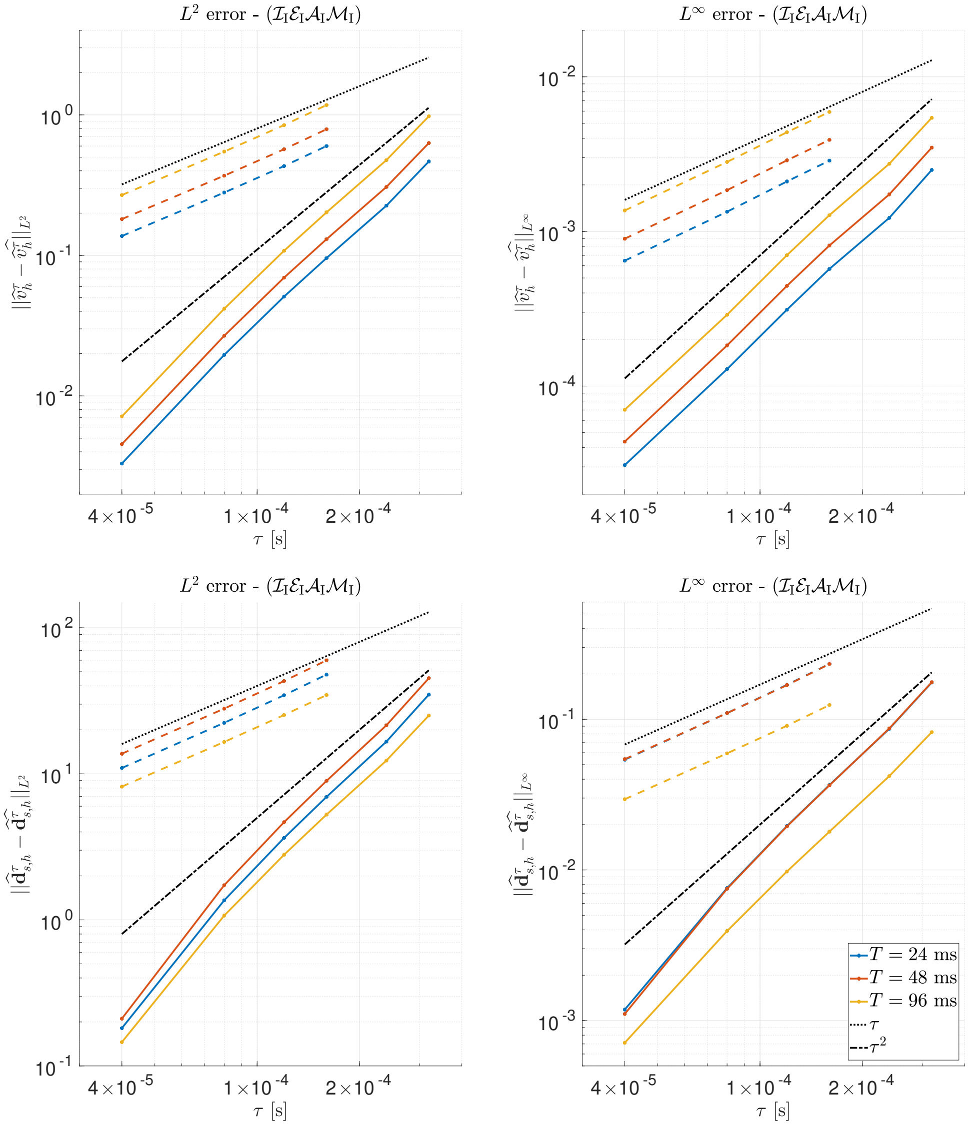

Figure 7: Errors in $L^2(\Omega_0)$ (left) and $L^\infty(\Omega_0)$ (right) norms of the potentials $\widehat{v}_h^\tau$ (top) and of the displacements $\widehat{\mathbf{d}}_h^\tau$ (bottom) obtained by solving the problem with the monolithic scheme $(\mathcal{I}_\text{I}\mathcal{E}_\text{I}\mathcal{A}_\text{I}\mathcal{M}_\text{I})$, at times $T = 24$ ms (blue), $T = 48$ ms (red), and $T = 96$ ms (yellow), in logarithmic scale against τ. The results for both BDF1 and BDF2 are reported.

In the following, we denote by $\widehat{v}_h^\tau$ and $\widehat{\mathbf{d}}_h^\tau$ the potential and the displacement solutions, respectively, obtained with $(\mathcal{I}_\text{I}\mathcal{E}_\text{I}\mathcal{A}_\text{I}\mathcal{M}_\text{I})$ and timestep τ, while we set $\widehat{\tau} = 10^{-5}$ s (the smallest timestep size used). We use the solution obtained by using $(\mathcal{I}_\text{I}\mathcal{E}_\text{I}\mathcal{A}_\text{I}\mathcal{M}_\text{I})$ with

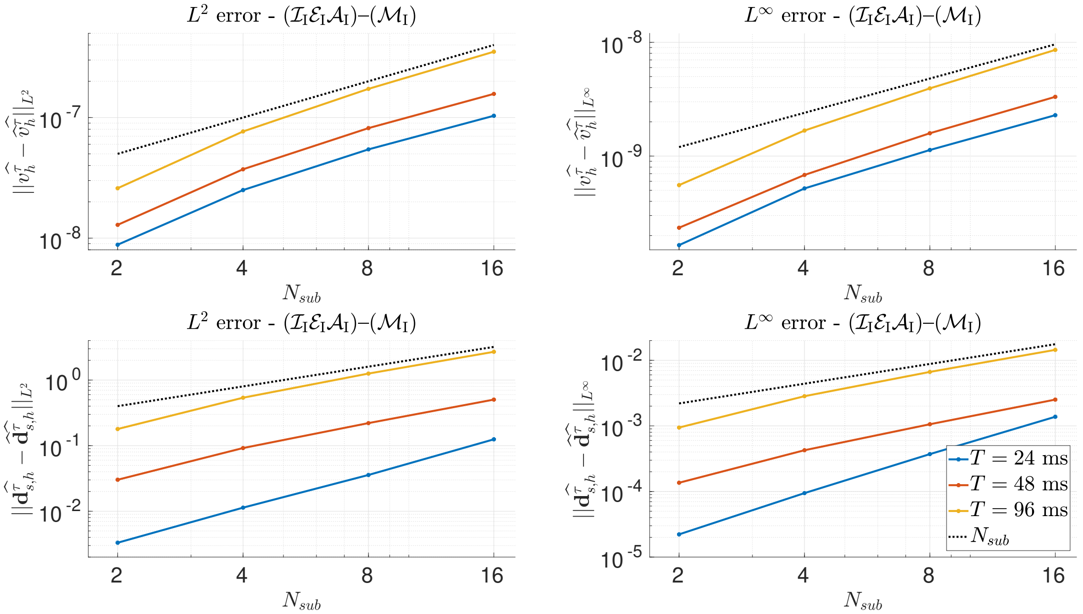

Figure 8: Errors in $L^2(\Omega_0)$ (left) and $L^\infty(\Omega_0)$ (right) norms of the potentials $v_h^{\widehat{\tau}}$ (top) and of the displacements $\mathbf{d}_h^{\widehat{\tau}}$ (bottom) at time $T = 96$ ms obtained by solving the problem with the segregated scheme $(\mathcal{I}_\mathrm{I}\mathcal{E}_\mathrm{I}\mathcal{A}_\mathrm{I})$–$(\mathcal{M}_\mathrm{I})$ and timestep τ, in logarithmic scale against N_{sub}.

$(\tau = \widehat{\tau})$ as a reference one (a manufactured "exact" solution). Indeed, since no exact solution for the electromechanics problem is available, the error analysis with respect to the timesteps is carried out by using a reference solution on the same mesh, effectively disregarding the error due to the space discretization. In the monolithic case, all the coupling conditions between the core models are enforced in the extradiagonal blocks of the monolithic system matrix. However, as we will show, this accuracy comes at the price of a large computational cost. In Figure 6 we report the deformation and the displacement field of the ideal geometry obtained by solving the problem with $(\mathcal{I}_\mathrm{I}\mathcal{E}_\mathrm{I}\mathcal{A}_\mathrm{I}\mathcal{M}_\mathrm{I})$ compared with the reference domain Ω_0.

We first numerically verify that in the $(\mathcal{I}_\mathrm{I}\mathcal{E}_\mathrm{I}\mathcal{A}_\mathrm{I}\mathcal{M}_\mathrm{I})$ case the errors in $L^2(\Omega_0)$ and $L^\infty(\Omega_0)$ norms of the potential and of the displacement magnitude decay as τ and τ^2 when using BDF with $\sigma = 1$ and $\sigma = 2$, respectively. With this aim, we display in Figure 7 the errors $||\widehat{v}_h^{\tau} - \widehat{v}_h^{\widehat{\tau}}||$ and $||\widehat{\mathbf{d}}_h^{\tau} - \widehat{\mathbf{d}}_h^{\widehat{\tau}}||$ against the timestep $\tau = \Delta t$. The converge rate is indeed coherent with the order σ of the BDF scheme under use.

Before analyzing the convergence rates against τ for the segregated schemes, we investigate the role of the splitting scheme on the mechanical feedback in the monodomain equation, which is realized by the dependence of the diffusion tensor on the deformation gradient $\mathbf{F}$. To this aim, we display in Figure 8 the errors, at times $T = 24, 48, 96$ ms,

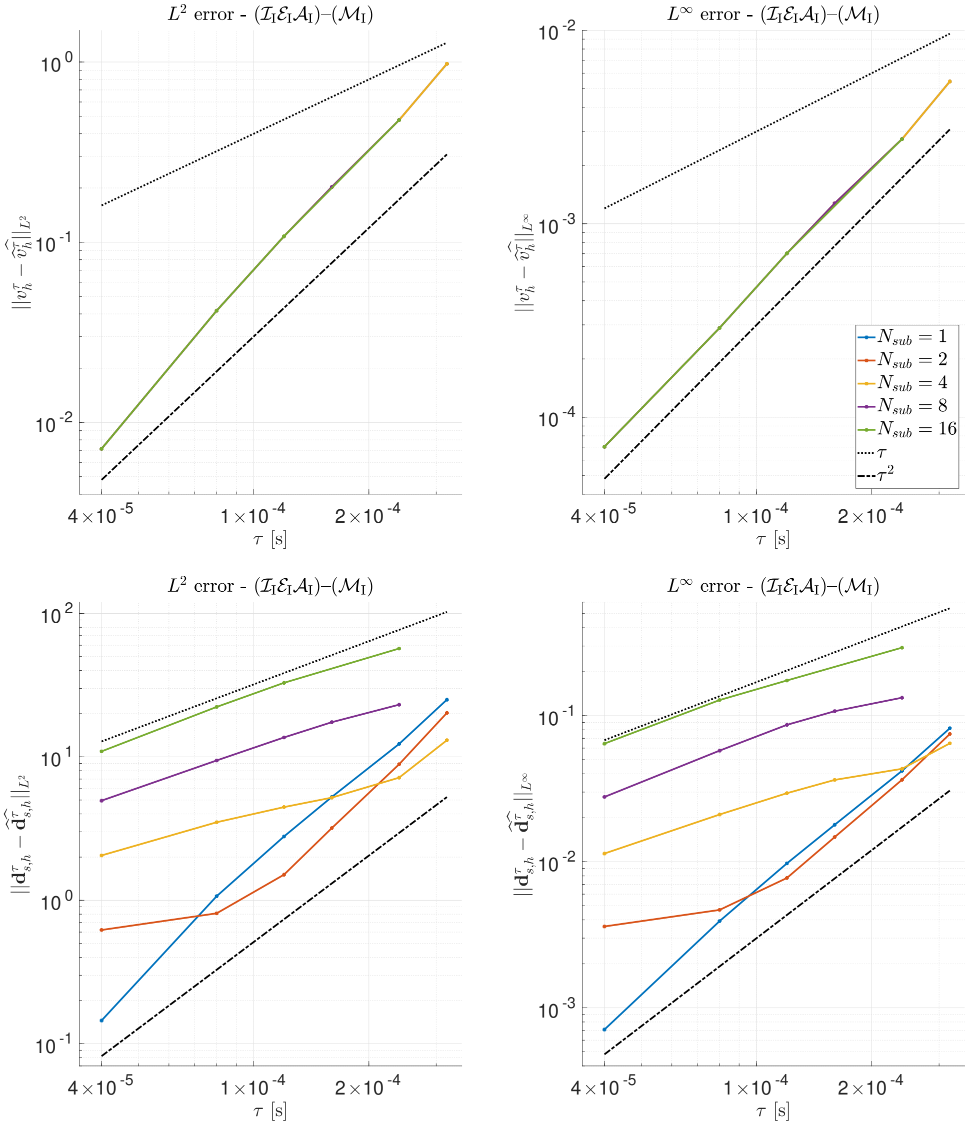

Figure 9: Errors in $L^2(\Omega_0)$ (left) and $L^\infty(\Omega_0)$ (right) norms of the potentials v_h^τ (top) and of the displacements $\mathbf{d}_h^\tau$ (bottom) at time $T = 96$ ms obtained by solving the problem with $(\mathcal{I}_{\mathrm{I}}\mathcal{E}_{\mathrm{I}}\mathcal{A}_{\mathrm{I}})$–$(\mathcal{M}_{\mathrm{I}})$ and $N_{sub} = 1, 2, 4, 8, 16$, in logarithmic scale against τ.

made using $(\mathcal{I}_{\mathrm{I}}\mathcal{E}_{\mathrm{I}}\mathcal{A}_{\mathrm{I}})$–$(\mathcal{M}_{\mathrm{I}})$ with $\widehat{\tau}$ for different values of the parameter N_{sub}. That is, we use $\tau = \widehat{\tau}$ for the electrophysiology and the activation – the same timestep used to obtain the reference solution – while using $\Delta t = N_{sub}\tau$ for the mechanics. We first of all observe that, in all cases, the convergence rate is linear with respect to N_{sub} (equivalently, with

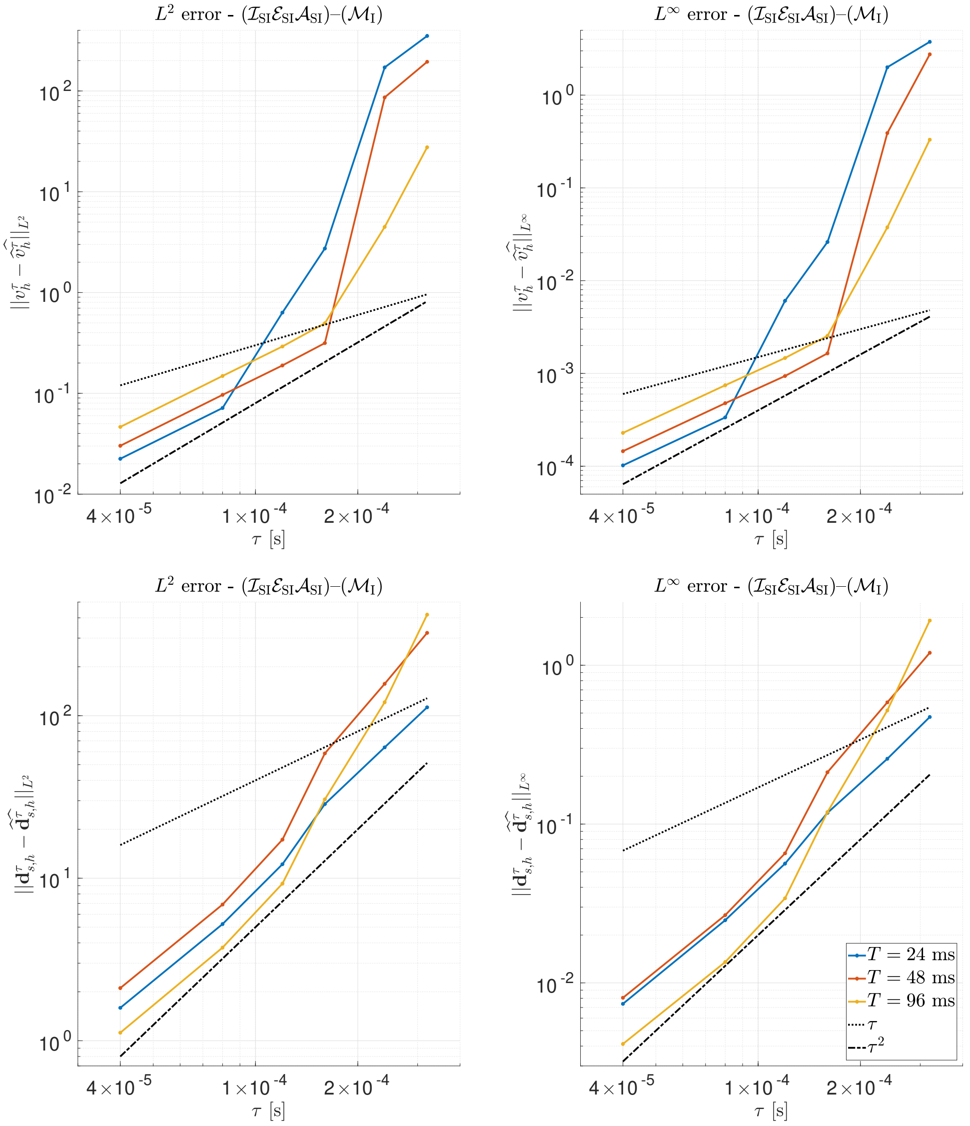

Figure 10: Errors in $L^2(\Omega_0)$ (left) and $L^\infty(\Omega_0)$ (right) norms of the potentials v_h^τ (top) and of the displacements $\mathbf{d}_h^\tau$ (bottom) obtained by solving the problem with $(\mathcal{I}_{\rm SI}\mathcal{E}_{\rm SI}\mathcal{A}_{\rm SI})$–$(\mathcal{M}_{\rm I})$, at times $T = 24$ ms (blue), $T = 48$ ms (red), and $T = 96$ ms (yellow), in logarithmic scale against τ, for $N_{sub} = 1$.

respect to Δt); this behavior is expected since the Godunov splitting scheme used in the segregated algorithm is first order accurate. Furthermore, while the magnitude of the error of the potential $\widehat{v}_h^\tau$ is negligible when compared to the errors in Figure 7, the same does

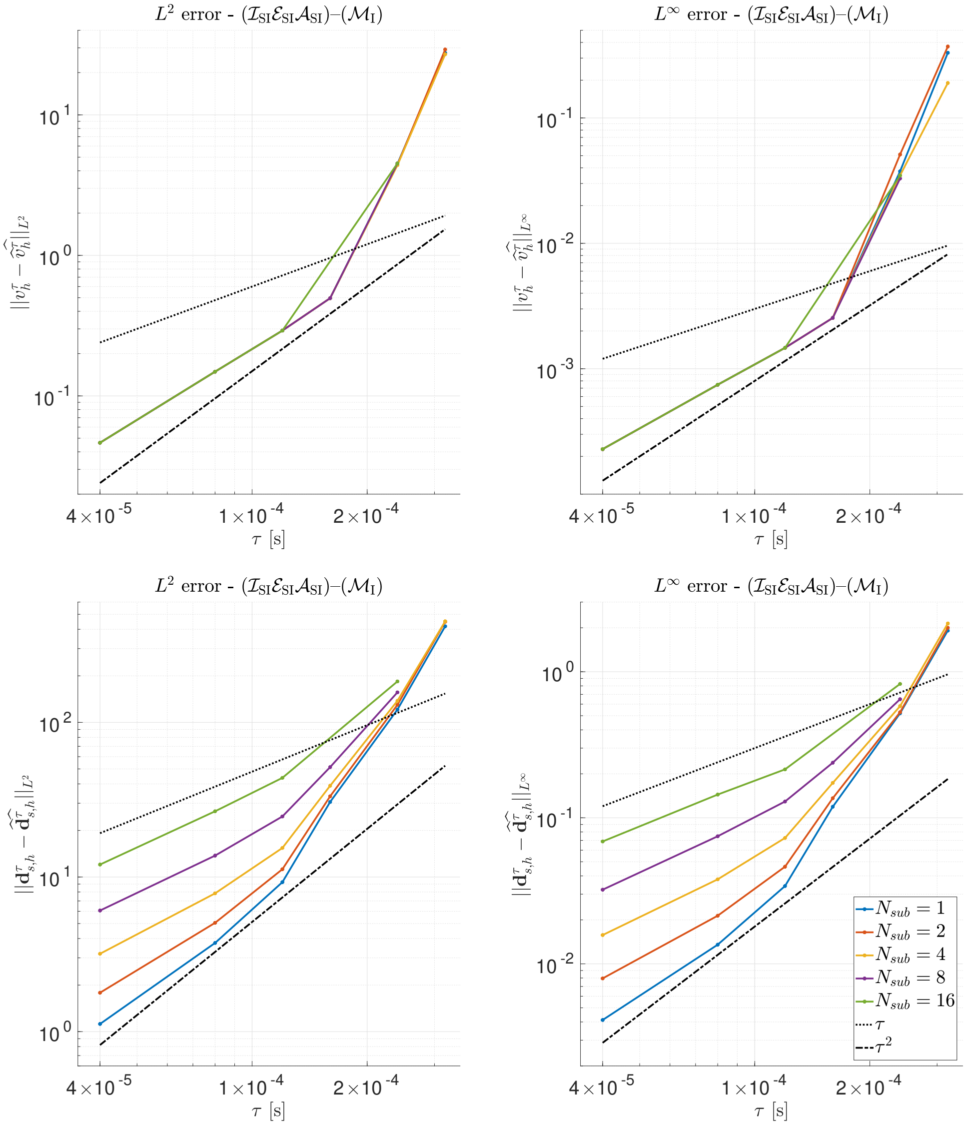

Figure 11: Errors in $L^2(\Omega_0)$ (left) and $L^\infty(\Omega_0)$ (right) norms of the potentials v_h^τ (top) and of the displacements $\mathbf{d}_h^\tau$ (bottom) at time $T = 96$ ms obtained by solving the problem with $(\mathcal{I}_{\rm SI}\mathcal{E}_{\rm SI}\mathcal{A}_{\rm SI})$–$(\mathcal{M}_{\rm I})$ and $N_{sub} = 1, 2, 4, 8, 16$, in logarithmic scale against τ.

not hold for the displacement $\mathbf{d}_h^{\widehat{\tau}}$. This is also expected since, in Figure 8, the value of τ is fixed while Δt is not, nonetheless this clearly shows that, for transmembrane potential, the splitting error is several orders of magnitude smaller than the one introduced when using a larger τ.

	$(\mathcal{I}_\mathrm{I}\mathcal{E}_\mathrm{I}\mathcal{A}_\mathrm{I}\mathcal{M}_\mathrm{I})$		
$\tau\ (=\Delta t)$	$\overline{N}^N$	$\overline{N}^G$	T^W
10^{-5} s	2.1	8.5	363'
2×10^{-5} s	2.4	8.1	188'
4×10^{-5} s	3.0	7.8	101'
8×10^{-5} s	3.5	7.7	54'
12×10^{-5} s	3.6	7.9	36'
16×10^{-5} s	4.0	7.6	28'
24×10^{-5} s	4.7	7.9	22'
32×10^{-5} s	5.2	9.2	18'

Table 1: The average number of Newton ($\overline{N}^N$) and GMRES ($\overline{N}^G$) iterations for the solution of the monolithic problem $(\mathcal{I}_\mathrm{I}\mathcal{E}_\mathrm{I}\mathcal{A}_\mathrm{I}\mathcal{M}_\mathrm{I})$, and the total wall time (T^W, in minutes) for the benchmark simulations, for each $\tau\ (=\Delta t)$ considered.

We then analyze the errors introduced when using $(\mathcal{I}_\mathrm{I}\mathcal{E}_\mathrm{I}\mathcal{A}_\mathrm{I})$–$(\mathcal{M}_\mathrm{I})$, $(\mathcal{I}_\mathrm{SI}\mathcal{E}_\mathrm{SI}\mathcal{A}_\mathrm{SI})$–$(\mathcal{M}_\mathrm{I})$, and $(\mathcal{I}_\mathrm{SI})$–$(\mathcal{E}_\mathrm{SI})$–$(\mathcal{A}_\mathrm{SI})$–$(\mathcal{M}_\mathrm{I})$ for varying τ and N_{sub}. We do not report the ones for the case $N_{sub}=1$ against τ (as previously done for the monolithic strategy) neither for $(\mathcal{I}_\mathrm{I}\mathcal{E}_\mathrm{I}\mathcal{A}_\mathrm{I})$–$(\mathcal{M}_\mathrm{I})$ nor for $(\mathcal{I}_\mathrm{SI})$–$(\mathcal{E}_\mathrm{SI})$–$(\mathcal{A}_\mathrm{SI})$–$(\mathcal{M}_\mathrm{I})$ since no appreciable differences are visible with respect to $(\mathcal{I}_\mathrm{I}\mathcal{E}_\mathrm{I}\mathcal{A}_\mathrm{I}\mathcal{M}_\mathrm{I})$ and $(\mathcal{I}_\mathrm{SI}\mathcal{E}_\mathrm{SI}\mathcal{A}_\mathrm{SI})$–$(\mathcal{M}_\mathrm{I})$, respectively. In Figure 9 the errors for the scheme $(\mathcal{I}_\mathrm{I}\mathcal{E}_\mathrm{I}\mathcal{A}_\mathrm{I})$–$(\mathcal{M}_\mathrm{I})$ at time $T=96$ ms are reported for different choices of N_{sub}. As previously mentioned, only first order accuracy is granted by the considered splitting schemes, however the error on the potential v_h^τ converges even quadratically (it is superconvergent). On the other hand, the error on the displacement $\mathbf{d}_h^\tau$ converges linearly, unless the values $N_{sub}=1,2$ are employed.

By considering now the $(\mathcal{I}_\mathrm{SI}\mathcal{E}_\mathrm{SI}\mathcal{A}_\mathrm{SI})$–$(\mathcal{M}_\mathrm{I})$ strategy, we report in Figure 10 the errors made for the potential and the displacement at times $T=24,48,96$ ms. We observe that the error significantly increases for $\tau > 8\times10^{-5}$ s, in particular for the potential v_h^τ. This is due to numerical instabilities occuring when using the semi-implicit case, which is "not guaranteed" to be stable for an arbitrary choice of τ. Nonetheless, these instabilities are "non-destructive" since the error on $\mathbf{d}_h^\tau$ is not significantly affected by them. However, in both cases, we observe again that the errors are superconvergent for $N_{sub}=1$ and $\tau \leq 8\times10^{-5}$ s as they decrease quadratically. We conclude our error analysis by reporting in Figure 11 the errors against Δt at time $T=96$ ms when using $(\mathcal{I}_\mathrm{SI}\mathcal{E}_\mathrm{SI}\mathcal{A}_\mathrm{SI})$–$(\mathcal{M}_\mathrm{I})$, for different choices of N_{sub}. We conclude that, similarly to the $(\mathcal{I}_\mathrm{I}\mathcal{E}_\mathrm{I}\mathcal{A}_\mathrm{I})$–$(\mathcal{M}_\mathrm{I})$ case, the errors converge at least linearly, as expected by the splitting schemes employed.

We now investigate the efficiency of the schemes as a function of τ and N_{sub}. In Tables 1-2 we report the average number of Newton ($\overline{N}^N$) and GMRES ($\overline{N}^N$) iterations required for the solution of the monolithic problem with $(\mathcal{I}_\mathrm{I}\mathcal{E}_\mathrm{I}\mathcal{A}_\mathrm{I}\mathcal{M}_\mathrm{I})$, and for the solution of the me-

	$(\mathcal{I}_{\mathrm{I}}\mathcal{E}_{\mathrm{I}}\mathcal{A}_{\mathrm{I}})$–$(\mathcal{M}_{\mathrm{I}})$														
	$N_{sub} = 1$			$N_{sub} = 2$			$N_{sub} = 4$			$N_{sub} = 8$			$N_{sub} = 16$		
τ	$\overline{N}^N$	$\overline{N}^G$	T^W	$\overline{N}^N$	$\overline{N}^G$	T^W	$\overline{N}^N$	$\overline{N}^G$	T^W	$\overline{N}^N$	$\overline{N}^G$	T^W	$\overline{N}^N$	$\overline{N}^G$	T^W
1	2.5	4.4	300’	2.7	4.7	221’	2.8	5.6	178’	3.3	5.4	156’	3.6	7.0	144’
2	2.7	4.7	144’	2.8	5.6	101’	3.3	5.4	81’	3.6	7.0	69’	4.1	10.3	63’
4	2.8	5.6	70’	3.3	5.4	50’	3.6	7.0	38’	4.1	10.2	32’	4.5	14.5	29’
8	3.3	5.4	38’	3.6	7.0	26’	4.1	10.3	20’	4.4	14.6	16’	5.2	18.7	15’
12	3.4	6.2	26’	3.8	8.8	18’	4.4	12.6	13’	4.8	17.2	11’	5.4	21.9	10’
16	3.6	7.0	20’	4.2	10.2	14’	4.4	14.6	10’	5.2	18.7	9’	5.5	24.7	8’
24	3.8	8.9	15’	4.4	12.6	10’	4.8	17.2	8’	5.4	21.9	6’	6.0	28.8	6’
32	4.2	10.3	12’	4.5	14.6	8’	5.3	18.7	6’	5.5	24.8	5’	6.0	33.2	5’

	$(\mathcal{I}_{\mathrm{SI}}\mathcal{E}_{\mathrm{SI}}\mathcal{A}_{\mathrm{SI}})$–$(\mathcal{M}_{\mathrm{I}})$														
	$N_{sub} = 1$			$N_{sub} = 2$			$N_{sub} = 4$			$N_{sub} = 8$			$N_{sub} = 16$		
τ	$\overline{N}^N$	$\overline{N}^G$	T^W	$\overline{N}^N$	$\overline{N}^G$	T^W	$\overline{N}^N$	$\overline{N}^G$	T^W	$\overline{N}^N$	$\overline{N}^G$	T^W	$\overline{N}^N$	$\overline{N}^G$	T^W
1	2.5	4.4	258’	2.7	4.7	179’	2.8	5.6	137’	3.3	5.4	115’	3.6	7.0	107’
2	2.7	4.7	123’	2.8	5.6	81’	3.3	5.4	59’	3.6	7.0	48’	4.1	10.2	42’
4	2.8	5.6	60’	3.3	5.4	39’	3.6	7.0	27’	4.2	10.2	21’	4.5	14.5	18’
8	3.3	5.4	32’	3.6	7.0	20’	4.1	10.2	14’	4.5	14.5	10’	5.2	18.6	8’
12	3.4	6.2	22’	3.9	8.8	13’	4.4	12.5	9’	4.8	17.1	7’	5.4	21.8	5’
16	3.5	7.0	16’	4.1	10.2	10’	4.4	14.5	7’	5.2	18.6	5’	5.5	24.6	4’
24	3.7	8.7	11’	4.3	12.3	7’	4.7	16.9	4’	5.3	21.5	3’	6.0	28.4	2’
32	3.8	9.9	8’	4.3	13.9	5’	4.8	18.5	3’	5.3	23.9	2’	10.6	23.9	2’

	$(\mathcal{I}_{\mathrm{SI}})$–$(\mathcal{E}_{\mathrm{SI}})$–$(\mathcal{A}_{\mathrm{SI}})$–$(\mathcal{M}_{\mathrm{I}})$														
	$N_{sub} = 1$			$N_{sub} = 2$			$N_{sub} = 4$			$N_{sub} = 8$			$N_{sub} = 16$		
τ	$\overline{N}^N$	$\overline{N}^G$	T^W	$\overline{N}^N$	$\overline{N}^G$	T^W	$\overline{N}^N$	$\overline{N}^G$	T^W	$\overline{N}^N$	$\overline{N}^G$	T^W	$\overline{N}^N$	$\overline{N}^G$	T^W
1	2.5	3.2	242’	2.7	3.6	159’	2.8	4.4	118’	3.3	4.4	97’	3.6	5.8	84’
2	2.7	3.6	114’	2.8	4.5	71’	3.3	4.5	50’	3.6	5.8	38’	4.1	8.5	32’
4	2.8	4.5	57’	3.3	4.5	36’	3.6	5.8	24’	4.2	8.5	18’	4.5	12.2	14’
8	3.3	4.5	31’	3.6	5.9	18’	4.2	8.6	12’	4.5	12.2	8’	5.2	15.9	7’
12	3.4	6.0	21’	3.8	8.0	13’	4.4	11.1	8’	4.8	15.2	6’	5.4	19.6	4’
16	3.5	7.0	16’	4.1	10.1	10’	4.4	14.3	6’	5.2	18.3	4’	5.5	24.3	3’
24	3.7	8.2	11’	4.3	11.6	6’	4.6	15.7	4’	5.4	20.2	3’	6.0	26.7	2’
32	3.8	8.5	8’	4.3	12.0	5’	4.8	15.9	3’	5.4	20.5	2’	9.8	28.7	1’

Table 2: The average number of Newton ($\overline{N}^N$) and GMRES ($\overline{N}^G$) iterations for the solution of the mechanics problem and the total wall time (T^W, in minutes) for the benchmark simulations, for each segregated strategy, τ (in 10^{-5} s), and N_{sub} considered.

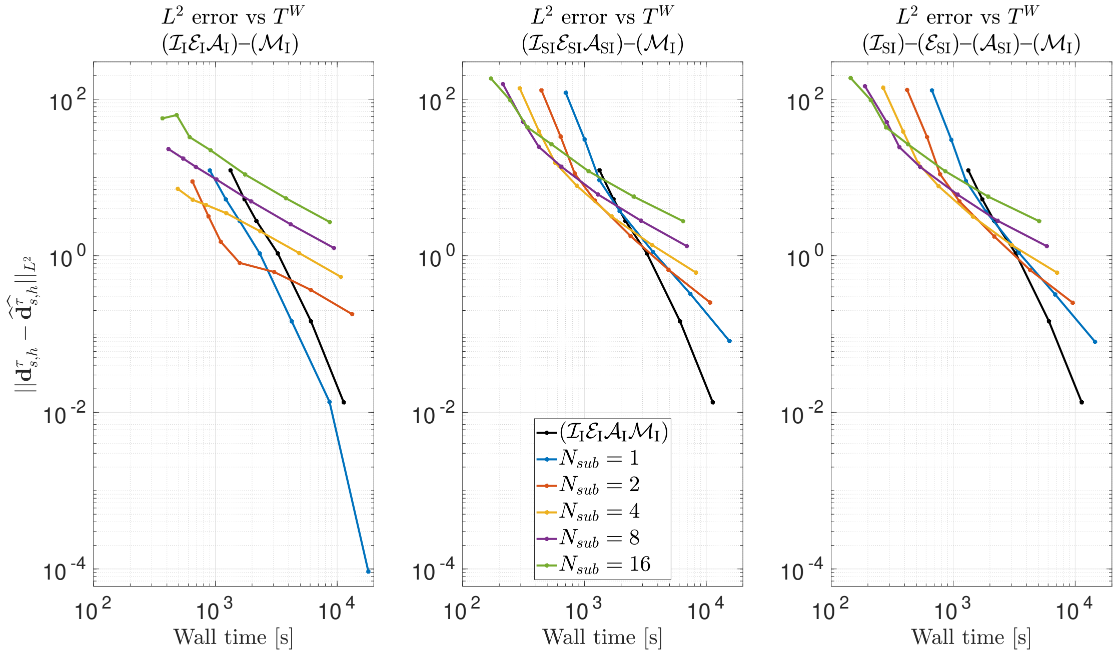

Figure 12: Errors in $L^2(\Omega)$ norm of the displacement at time $T = 96$ ms against the total wall time T^W for the $(\mathcal{I}_{\mathrm{I}}\mathcal{E}_{\mathrm{I}}\mathcal{A}_{\mathrm{I}})$–$(\mathcal{M}_{\mathrm{I}})$, $(\mathcal{I}_{\mathrm{SI}}\mathcal{E}_{\mathrm{SI}}\mathcal{A}_{\mathrm{SI}})$–$(\mathcal{M}_{\mathrm{I}})$, and $(\mathcal{I}_{\mathrm{SI}})$–$(\mathcal{E}_{\mathrm{SI}})$–$(\mathcal{A}_{\mathrm{SI}})$–$(\mathcal{M}_{\mathrm{I}})$ strategies for $N_{sub} = 1, 2, 4, 8, 16$, compared to the error for the $(\mathcal{I}_{\mathrm{I}}\mathcal{E}_{\mathrm{I}}\mathcal{A}_{\mathrm{I}}\mathcal{M}_{\mathrm{I}})$ strategy.

chanics problem with the $(\mathcal{I}_{\mathrm{I}}\mathcal{E}_{\mathrm{I}}\mathcal{A}_{\mathrm{I}})$–$(\mathcal{M}_{\mathrm{I}})$, $(\mathcal{I}_{\mathrm{SI}}\mathcal{E}_{\mathrm{SI}}\mathcal{A}_{\mathrm{SI}})$–$(\mathcal{M}_{\mathrm{I}})$, and $(\mathcal{I}_{\mathrm{SI}})$–$(\mathcal{E}_{\mathrm{SI}})$–$(\mathcal{A}_{\mathrm{SI}})$–$(\mathcal{M}_{\mathrm{I}})$ strategies. As expected, both $\overline{N}^N$ and $\overline{N}^G$ increase significantly as τ gets larger and larger. Otherwise, the required wall time T^W dramatically drops with a speed-up of almost 300 times when using the strategy $(\mathcal{I}_{\mathrm{SI}})$–$(\mathcal{E}_{\mathrm{SI}})$–$(\mathcal{A}_{\mathrm{SI}})$–$(\mathcal{M}_{\mathrm{I}})$ and timestep $\tau = 32 \times 10^{-5}$, with respect to $(\mathcal{I}_{\mathrm{I}}\mathcal{E}_{\mathrm{I}}\mathcal{A}_{\mathrm{I}}\mathcal{M}_{\mathrm{I}})$ and timestep $\tau = 1 \times 10^{-5}$.

We can now better compare the efficiency of the different strategies by displaying in Figure 12 the errors of the displacement in $L^2(\Omega)$ norm against the total wall time T^W, and hence establish which strategy is the most efficient for a given tolerance on the error. The first clear conclusion that can be drawn is that, for any tolerance, it is more convenient to use the $(\mathcal{I}_{\mathrm{I}}\mathcal{E}_{\mathrm{I}}\mathcal{A}_{\mathrm{I}})$–$(\mathcal{M}_{\mathrm{I}})$ strategy with $N_{sub} = 1$ rather than the monolithic $(\mathcal{I}_{\mathrm{I}}\mathcal{E}_{\mathrm{I}}\mathcal{A}_{\mathrm{I}}\mathcal{M}_{\mathrm{I}})$ one; this is in agreement with our previous observations on the magnitude of the splitting error introduced by using the $(\mathcal{I}_{\mathrm{I}}\mathcal{E}_{\mathrm{I}}\mathcal{A}_{\mathrm{I}})$–$(\mathcal{M}_{\mathrm{I}})$ strategy. More in general, we observe that the proposed segregated strategies represent a better alternative with respect to the monolithic one if a larger error on the displacement is deemed to be acceptable. We conclude that the chosen strategy represents a trade-off between the efficiency of the simulation and the accuracy of the approximated solution. If the goal is that of reducing the computational cost, the $(\mathcal{I}_{\mathrm{SI}})$–$(\mathcal{E}_{\mathrm{SI}})$–$(\mathcal{A}_{\mathrm{SI}})$–$(\mathcal{M}_{\mathrm{I}})$ strategy should be the matter of choice, although its

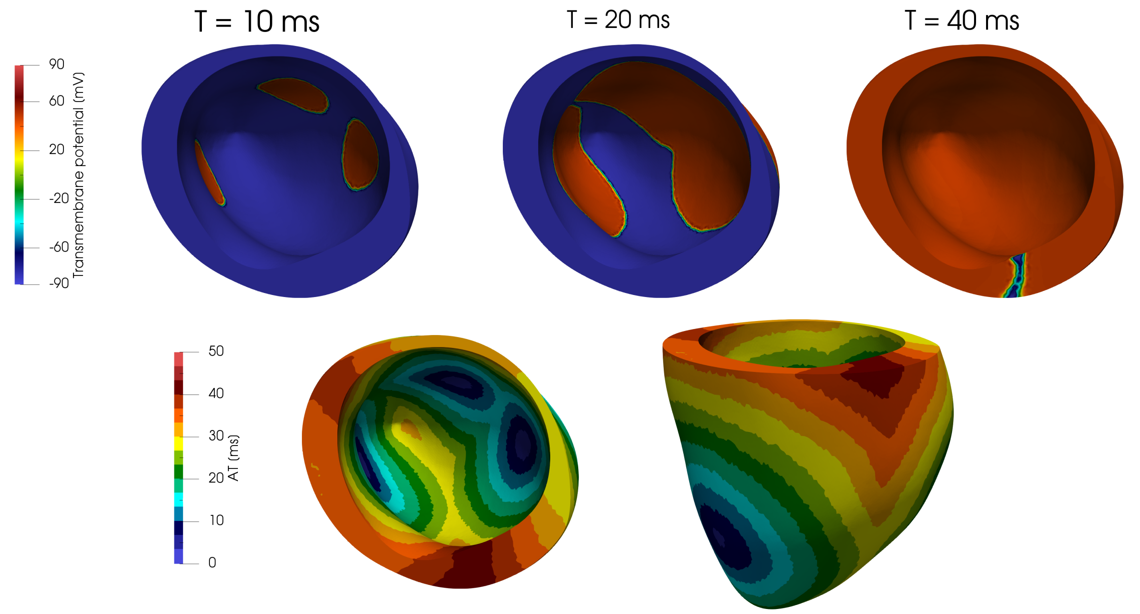

Figure 13: Transmembrane potential at different times (top row) and activation time (bottom row) for the subject-specific simulation.

accuracy drops for larger timestep sizes. On the other hand, if accuracy is the driving factor, $(\mathcal{I}_{\mathrm{I}}\mathcal{E}_{\mathrm{I}}\mathcal{A}_{\mathrm{I}})$–$(\mathcal{M}_{\mathrm{I}})$ has to be preferred to $(\mathcal{I}_{\mathrm{I}}\mathcal{E}_{\mathrm{I}}\mathcal{A}_{\mathrm{I}}\mathcal{M}_{\mathrm{I}})$ thus avoiding the extremely long wall times needed by the latter.

5.3 Subject-specific LV: the full heartbeat

We use the subject-specific mesh of Figure 5 for the simulation of a full heartbeat by modeling the pressure as detailed in Section 3.2.1 and by setting $T = 0.8$ s. Basis functions of degree $r = 1$ are employed, thus obtaining a system of size $M = 8 \times N_1^{dof} = 1'008'248$ in the monolithic case, together with BDF of order $\sigma = 2$. The timestep is set equal to $\tau = 5 \times 10^{-5}$ s while $\Delta t = N_{sub}\tau$ with $N_{sub} = 1, 5, 10$ for the segregated strategies. All the numerical simulations were carried out using Piz Daint, a Cray XC50/XC40 supercomputer installed at the Swiss National Supercomputing Center (CSCS)[3], and a total number of 72 cores was used for each simulation[4].

---

[3] http://www.cscs.ch

[4] Unfortunately the maximum wall time allowed on the Piz Daint supercomputer is set to 24 hours, thus making it impossible to complete a simulation of a full heartbeat in all cases - most notably for the $(\mathcal{I}_{\mathrm{I}}\mathcal{E}_{\mathrm{I}}\mathcal{A}_{\mathrm{I}}\mathcal{M}_{\mathrm{I}})$ strategy, which is the most computational demanding. We hence run two sets of simulations: in the first case, we set $T = 0.8$ s thus obtaining the pressure-volume loops of Figure 16; in the second one, we set $T = 0.073$ s (the maximum time reacheable in 24 hours with the $(\mathcal{I}_{\mathrm{I}}\mathcal{E}_{\mathrm{I}}\mathcal{A}_{\mathrm{I}}\mathcal{M}_{\mathrm{I}})$ strategy) thus

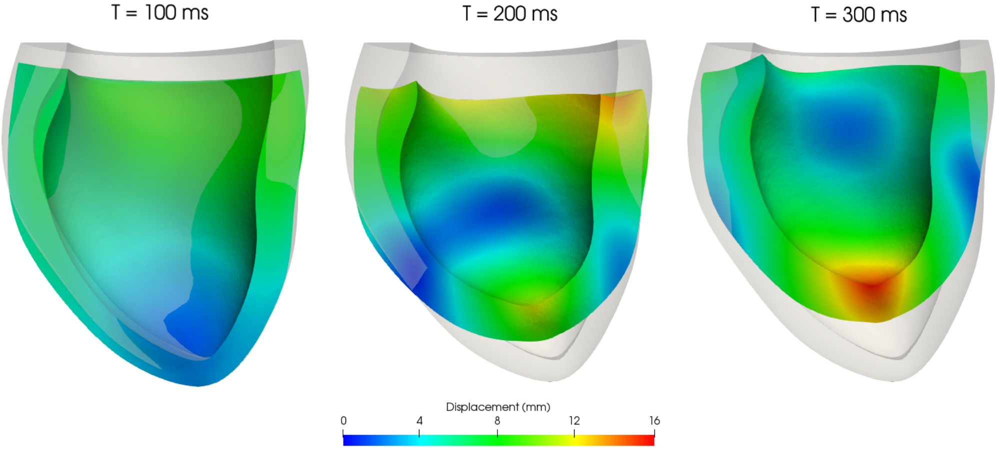

Figure 14: Deformed subject-specific geometry and displacement field at different times, compared with the reference domain Ω_0, for the full heartbeat simulation.

As for the previous test, a current is applied at the endocardium at three distinct points for 3 ms in order to trigger the cardiac rythm. We show the results obtained in Figure 13, where the transmembrane potential at times $T = 10, 20, 40$ ms is depicted together with the activation time (AT). The latter is defined, in each point, as the time at which the electric potential reaches a threshold value v^{thr} (we set in particular $v^{thr} = 10$ mV) [56, 81]. The activation time is in good agreement with experimental data obtained from healthy patients [10, 82], since the complete activation of the myocardium takes around 40 ms.

In Figure 14 we show the displacement magnitude on the deformed myocardium Ω, compared with the reference geometry Ω_0, at the times $T = 100, 200, 300$ ms. A significant thickening of the myocardium walls takes place, which is in accordance with experimental observations [63]. The model, however, only produces a moderate rotation of the LV: in [58] the authors suggest that this behavior is related to the choice of the incompressibility constraint, the bulk modulus B magnitude, and to the boundary conditions. In order to better appreciate the behavior of the employed model, we also estimate the components of the stress tensor in the fibers and sheets direction $\sigma_{ff} = (\mathbf{P}\mathbf{f}_0)\mathbf{f}$ and $\sigma_{ss} = (\mathbf{P}\mathbf{s}_0)\mathbf{s}$. With

---

obtaining the results of Table 16.

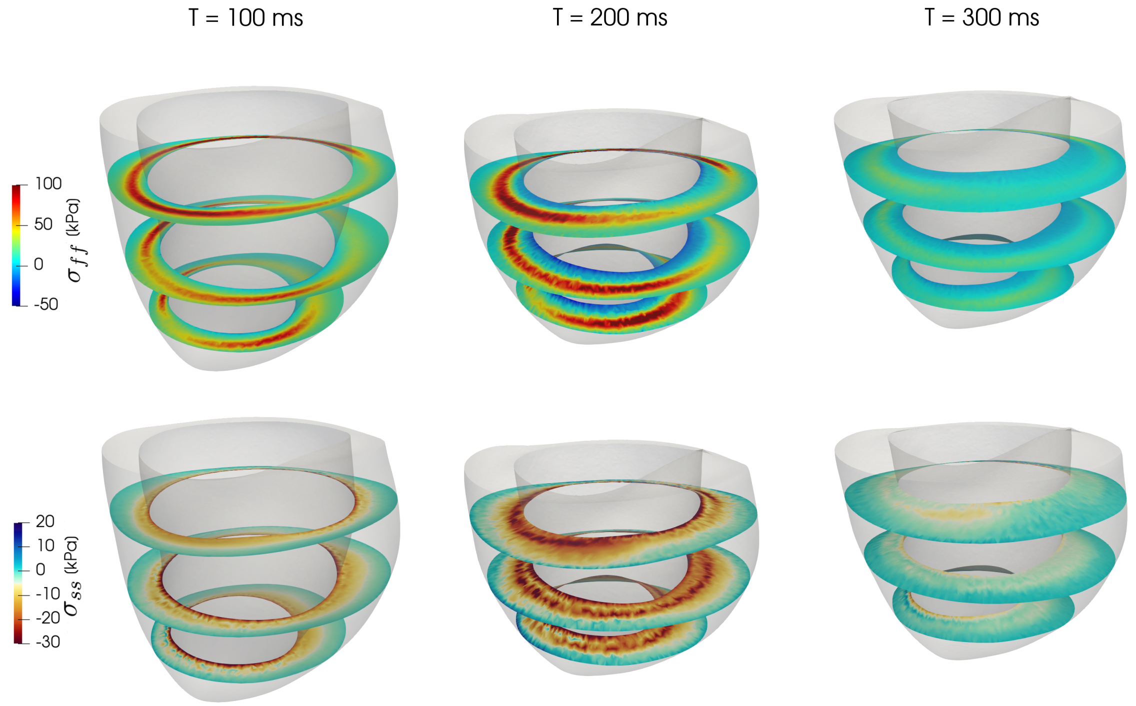

Figure 15: Stress components σ_{ff} (top) and σ_{ss} (bottom) depicted on three slices of the deformed domain at three different times.

this aim, we solve the following L^2-projection problem: find σ_{ff} such that

$$\int_{\Omega_0} \sigma_{ff}\psi_i = \int_{\Omega_0} (\mathbf{P}\mathbf{f}_0)\mathbf{f}\psi_i,$$

for $i, \dots, N_1^{\text{dof}}$, and analogously for σ_{ss}. In Figure 15 we show the two fields obtained at the same times considered in Figure 14; we highlight that $T = 200$ ms corresponds approximately to the time at which the LV pressure attains its maximum (around 120 mmHg). The values assumed by σ_{ss} mostly fall in the physiological range [39, 75, 85, 87] and match the pressure value at the endocardium. Nonetheless the stress value peaks in the region close to the myocardium base; we believe that this is due to the thickness of the septum wall which, in this subject-specific geometry, was reconstructed as particularly thin. Regarding the stress σ_{ff}, the model reproduces much larger values with respect to those indicated in [6, 39, 87], thus overestimating them by almost an order of magnitude especially where the myocardium wall is (much) thinner. We remark, however, that the available medical data used in [39] to fit the strain energy function is obtained with in vitro loading tests, hence accounting only for the passive component of the stress.

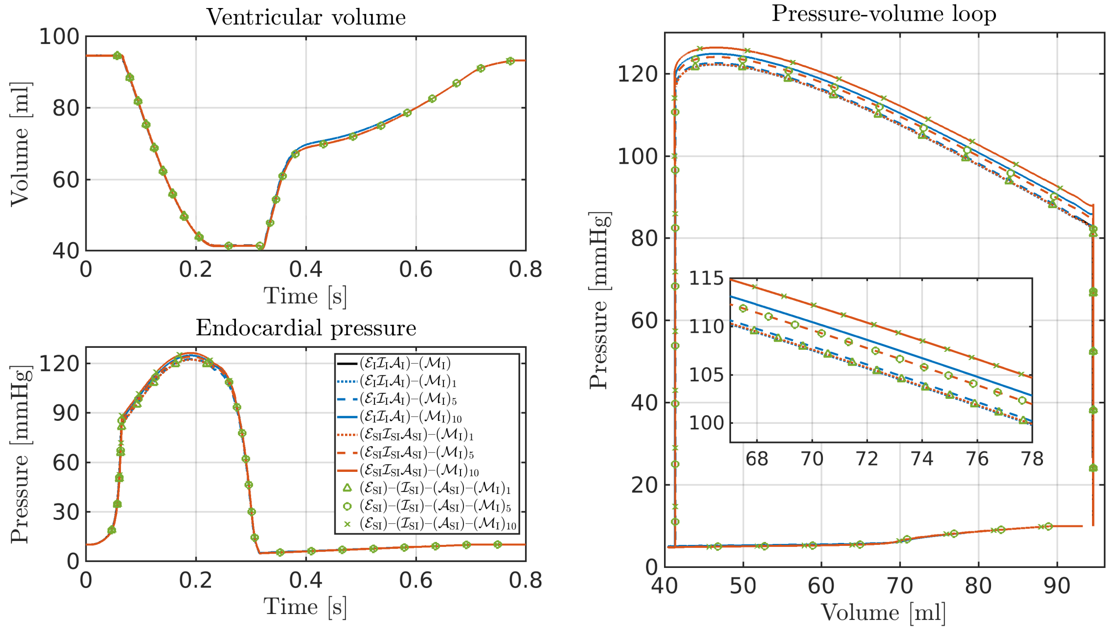

Figure 16: LV internal volumes (top left) and endocardial pressures (bottom left) versus time, with pV loops (right) for the subject-specific simulations with all the strategies considered (the parameter N_{sub} used is indicated in legend with a subscript).

Finally, we compare in Figure 16 the pressure-volume (pV) loops obtained with the different numerical coupling strategies. A close up of the pV loops in the ejection phase is also reported to better assess the differences among them. We observe that, as in the benchmark test, the difference between the results obtained with $(\mathcal{I}_{\rm SI}\mathcal{E}_{\rm SI}\mathcal{A}_{\rm SI})$–$(\mathcal{M}_{\rm I})$ and those obtained with $(\mathcal{I}_{\rm SI})$–$(\mathcal{E}_{\rm SI})$–$(\mathcal{A}_{\rm SI})$–$(\mathcal{M}_{\rm I})$ is negligible. We conclude that the main deviation among the pV loops is caused by the choice of different timestep lengths $\Delta t = N_{sub}\tau$ for the mechanical model. Specifically, during the last part of the first isovolumic phase, the endocardial pressure increases very rapidly, while the change of the phase (as detailed in Section 2.4) takes place when the condition $p^{endo} \geq p^{ao}$ is satisfied. Hence, when using a large mechanics timestep Δt, the value of the pressure is higher when the ejection phase begins.

We conclude the analysis of the subject-specific simulations by reporting in Table 3 the values of $\overline{N}^N$, $\overline{N}^G$, and T^W, for the simulation of the heartbeat with final time set to $T = 0.073$ for all the strategies used. We observe that, even if in this case the number of Newton and GMRES iterations increases significantly with respect to the benchmark simulation case, the segregated schemes, and in particular the staggered schemes, allow to greatly reduce the computational costs for the subject-specific simulations too. Indeed, a

Strategy	N_{sub}	Δt	$\overline{N}^N$	$\overline{N}^G$	T^W
$(\mathcal{I}_{\mathrm{I}}\mathcal{E}_{\mathrm{I}}\mathcal{A}_{\mathrm{I}}\mathcal{M}_{\mathrm{I}})$	-	5	3.3	18.7	1440’
$(\mathcal{I}_{\mathrm{I}}\mathcal{E}_{\mathrm{I}}\mathcal{A}_{\mathrm{I}})$–$(\mathcal{M}_{\mathrm{I}})$	1	10	4.4	40.8	723’
$(\mathcal{I}_{\mathrm{I}}\mathcal{E}_{\mathrm{I}}\mathcal{A}_{\mathrm{I}})$–$(\mathcal{M}_{\mathrm{I}})$	5	25	5.1	71.8	284’
$(\mathcal{I}_{\mathrm{I}}\mathcal{E}_{\mathrm{I}}\mathcal{A}_{\mathrm{I}})$–$(\mathcal{M}_{\mathrm{I}})$	10	50	5.8	93.6	259’
$(\mathcal{I}_{\mathrm{SI}}\mathcal{E}_{\mathrm{SI}}\mathcal{A}_{\mathrm{SI}})$–$(\mathcal{M}_{\mathrm{I}})$	1	10	4.4	40.8	543’
$(\mathcal{I}_{\mathrm{SI}}\mathcal{E}_{\mathrm{SI}}\mathcal{A}_{\mathrm{SI}})$–$(\mathcal{M}_{\mathrm{I}})$	5	25	5.0	72.1	136’
$(\mathcal{I}_{\mathrm{SI}}\mathcal{E}_{\mathrm{SI}}\mathcal{A}_{\mathrm{SI}})$–$(\mathcal{M}_{\mathrm{I}})$	10	50	5.7	93.7	130’
$(\mathcal{I}_{\mathrm{SI}})$–$(\mathcal{E}_{\mathrm{SI}})$–$(\mathcal{A}_{\mathrm{SI}})$–$(\mathcal{M}_{\mathrm{I}})$	1	10	4.4	37.7	582’
$(\mathcal{I}_{\mathrm{SI}})$–$(\mathcal{E}_{\mathrm{SI}})$–$(\mathcal{A}_{\mathrm{SI}})$–$(\mathcal{M}_{\mathrm{I}})$	5	25	5.1	66.1	148’
$(\mathcal{I}_{\mathrm{SI}})$–$(\mathcal{E}_{\mathrm{SI}})$–$(\mathcal{A}_{\mathrm{SI}})$–$(\mathcal{M}_{\mathrm{I}})$	10	50	5.7	86.4	93’

Table 3: The mechanics timestep Δt (in 10^{-5} s), the average number of Newton ($\overline{N}^N$) and GMRES ($\overline{N}^G$) iterations, and the total wall time (T^W, in minutes) for the simulation of the heartbeat with final time $T = 0.073$ s with the subject-specific mesh, using the four strategies considered and $N_{sub} = 1, 5, 10$.

speed-up of up to 16 times is obtained when using the $(\mathcal{I}_{\mathrm{SI}})$–$(\mathcal{E}_{\mathrm{SI}})$–$(\mathcal{A}_{\mathrm{SI}})$–$(\mathcal{M}_{\mathrm{I}})$ strategy with $N_{sub} = 10$, compared to $(\mathcal{I}_{\mathrm{I}}\mathcal{E}_{\mathrm{I}}\mathcal{A}_{\mathrm{I}}\mathcal{M}_{\mathrm{I}})$ used with the same timestep length τ.

6 Conclusions

In this work, we proposed several segregated strategies for the solution of the integrated electromechanics problem for the LV. We formulated the continuous model by coupling the monodomain equation, the ionic minimal model, the activation model for the fibers contraction, and the myocardial mechanics in the active strain framework. We approximated the mathematical model in space by means of the Finite Element method, and in time with both implicit and semi-implicit schemes based on BDF; then, we formulated segregated strategies for its solution, considering the more general case of staggered time discretizations arising from the choice of different timestep sizes for the electrophysiology and mechanical activation, and for the mechanics.

The proposed segregated strategies were used with an idealized geometry for the simulation of a free contraction benchmark. The error on the results were evaluated against the solution obtained with $(\mathcal{I}_{\mathrm{I}}\mathcal{E}_{\mathrm{I}}\mathcal{A}_{\mathrm{I}}\mathcal{M}_{\mathrm{I}})$ and $\tau = 10^{-5}$ s, here assumed to be almost “exact”. We concluded from our error analysis that an approach based on segregating the mechanics from the rest of the problem allows to significantly reduce the computational cost of the simulation while providing accurate results: in the benchmark setting, it was possible to reduce the wall time for a 0.1 seconds long contraction approximately from 6 hours with

$(\mathcal{I}_{\rm I}\mathcal{E}_{\rm I}\mathcal{A}_{\rm I}\mathcal{M}_{\rm I})$, to 2.5 hours with $(\mathcal{I}_{\rm I}\mathcal{E}_{\rm I}\mathcal{A}_{\rm I})$–$(\mathcal{M}_{\rm I})$ and $N_{sub} = 16$. Using a semi-implicit time scheme for the electrophysiology and the activation allows to further cut the time required for the simulation, but at relatively large timesteps – for which the semi-implicit scheme is not stable – the accuracy significantly drops. Then, we showed that if the electrophysiology and the activation are solved in a sequential fashion instead of a monolithic one, the computational cost further reduced while the accuracy is preserved. With this approach, by using $(\mathcal{I}_{\rm SI})$–$(\mathcal{E}_{\rm SI})$–$(\mathcal{A}_{\rm SI})$–$(\mathcal{M}_{\rm I})$ and $N_{sub} = 16$, we were able to solve the problem in less than 1.5 hours.

Finally, we showed that the same integrated model can be used for large scale simulations with subject-specific geometries. We used the proposed strategies for the simulation of a full heartbeat and showed that physiological values for the pressure and the volume, are obtained. Segregated algorithms exhibit a significantly improved efficiency in this case too, when compared to the monolithic one. We conclude that segregated strategies are preferable if a relatively low accuracy is acceptable, while the monolithic strategy should be preferred if the required accuracy is extremely high.

7 Acknowledgements

This research was partially supported by the Swiss Platform for Advanced Scientific Computing (PASC, project "Integrative HPC Framework for Coupled Cardiac Simulations"). We also gratefully acknowledge the Swiss National Supercomputing Center (CSCS) for providing the CPU resources for the numerical simulations under project IDs s635/s796.

We acknowledge Prof. J. Schwitter and Dr. P. Masci (CHUV, Lausanne) for providing the MRI images used in this work and for the enlightening discussions. We also thank Prof. P. Tozzi (CHUV, Lausanne) for the invaluable insights in the functioning of the human heart.

The second and third authors acknowledge the ERC Advanced Grant iHEART, "An Integrated Heart Model for the simulation of the cardiac function", 20172022, P.I. A. Quarteroni (ERC2016ADG, project ID: 740132).

References

[1] R.R. Aliev and A.V. Panfilov. A simple two-variable model of cardiac excitation. *Chaos, Solitons & Fractals*, 7(3):293–301, 1996.

[2] D. Ambrosi, G. Arioli, F. Nobile, and A. Quarteroni. Electromechanical coupling in cardiac dynamics: the active strain approach. *SIAM Journal on Applied Mathematics*, 71(2):605–621, 2011.

[3] D. Ambrosi and S. Pezzuto. Active stress vs. active strain in mechanobiology: constitutive issues. *Journal of Elasticity*, 107(2):199–212, 2012.

[4] C.M. Augustin, A. Neic, M. Liebmann, A.J. Prassl, S.A. Niederer, G. Haase, and G. Plank. Anatomically accurate high resolution modeling of human whole heart electromechanics: a strongly scalable algebraic multigrid solver method for nonlinear deformation. *Journal of Computational Physics*, 305:622–646, 2016.

[5] L. Barbarotta. A mathematical and numerical study of the left ventricular contraction based on the reconstruction of a patient specific geometry. Master thesis, Politecnico di Milano, Italy, 2014.

[6] L. Barbarotta, S. Rossi, L. Dedè, and A. Quarteroni. Numerical validation of a transmurally heterogeneous orthotropic activation model for ventricular contraction. *MOX report*, 62/2017, 2017.

[7] C. Brooks and H.H. Lu. *The sinoatrial pacemaker of the heart.* Charles C. Thomas Publisher, 1972.

[8] A. Bueno-Orovio, E.M. Cherry, and F.H. Fenton. Minimal model for human ventricular action potentials in tissue. *Journal of Theoretical Biology*, 253(3):544–560, 2008.

[9] E. Burman and A. Ern. The discrete maximum principle for stabilized finite element methods. In *Numerical Mathematics and Advanced Applications*, pages 557–566. Springer, 2003.

[10] D.M. Cassidy, J.A. Vassallo, F.E. Marchlinski, A.E. Buxton, W.J. Untereker, and M.E. Josephson. Endocardial mapping in humans in sinus rhythm with normal left ventricles: activation patterns and characteristics of electrograms. *Circulation*, 70(1):37–42, 1984.

[11] F.E. Cellier and E. Kofman. *Continuous System Simulation.* Springer Science & Business Media, 2006.

[12] D. Chapelle, M. Fernández, J.F. Gerbeau, P. Moireau, J. Sainte-Marie, and N. Zemzemi. Numerical simulation of the electromechanical activity of the heart. *Functional Imaging and Modeling of the Heart*, pages 357–365, 2009.

[13] P. Colli Franzone, L. F. Pavarino, and G. Savaré. Computational electrocardiology: mathematical and numerical modeling. In *Complex Systems in Biomedicine*, pages 187–241. Springer, 2006.

[14] P. Colli Franzone, L. F. Pavarino, and S. Scacchi. Bioelectrical effects of mechanical feedbacks in a strongly coupled cardiac electro-mechanical model. *Mathematical Models and Methods in Applied Sciences*, 26(01):27–57, 2016.

[15] P. Colli Franzone, L.F. Pavarino, and S. Scacchi. *Mathematical Cardiac Electrophysiology*, volume 13. Springer, 2014.

[16] P. Colli Franzone, L.F. Pavarino, and S. Scacchi. Parallel multilevel solvers for the cardiac electro-mechanical coupling. *Applied Numerical Mathematics*, 95:140–153, 2015.

[17] P. Colli Franzone, L.F. Pavarino, and S. Scacchi. Joint influence of transmural heterogeneities and wall deformation on cardiac bioelectrical activity: a simulation study. *Mathematical biosciences*, 280:71–86, 2016.

[18] P. Colli Franzone, L.F. Pavarino, and S. Scacchi. Effects of mechanical feedback on the stability of cardiac scroll waves: a bidomain electro-mechanical simulation study. *Chaos: An Interdisciplinary Journal of Nonlinear Science*, 27(9), 2017.

[19] F.S. Costabal, F.A Concha, D.E. Hurtado, and E. Kuhl. The importance of mechano-electrical feedback and inertia in cardiac electromechanics. *Computer Methods in Applied Mechanics and Engineering*, 320:352–368, 2017.

[20] H. Dal, S. Göktepe, M. Kaliske, and E. Kuhl. A three-field, bi-domain based approach to the strongly coupled electromechanics of the heart. *Proceedings in Applied Mathematics and Mechanics*, 11(1):931–934, 2011.

[21] H. Dal, S. Göktepe, M. Kaliske, and E. Kuhl. A fully implicit finite element method for bidomain models of cardiac electromechanics. *Computer Methods in Applied Mechanics and Engineering*, 253:323–336, 2013.

[22] M.J. Davis, J.A. Donovitz, and J.D. Hood. Stretch-activated single-channel and whole cell currents in vascular smooth muscle cells. *American Journal of Physiology-Cell Physiology*, 262(4):C1083–C1088, 1992.

[23] S. Deparis, D. Forti, P. Gervasio, and A. Quarteroni. INTERNODES: an accurate interpolation-based method for coupling the galerkin solutions of pdes on subdomains featuring non-conforming interfaces. *Computers & Fluids*, 141:22–41, 2016.

[24] S. Deparis, D. Forti, G. Grandperrin, and A. Quarteroni. FaCSI: A block parallel preconditioner for fluid-structure interaction in hemodynamics. *Journal of Computational Physics*, 327:700–718, 2016.

[25] S. Doll and K. Schweizerhof. On the development of volumetric strain energy functions. *Journal of Applied Mechanics*, 67(1):17–21, 2000.

[26] T.S.E. Eriksson, A.J. Prassl, G. Plank, and G.A. Holzapfel. Influence of myocardial fiber/sheet orientations on left ventricular mechanical contraction. *Mathematics and Mechanics of Solids*, 18(6):592–606, 2013.

[27] D. Forti, M. Bukac, A. Quaini, S. Canic, and S. Deparis. A monolithic approach to fluid–composite structure interaction. *Journal of Scientific Computing*, pages 1–26, 2016.

[28] A. Gerbi, L. Dedè, and A. Quarteroni. A monolithic algorithm for the simulation of cardiac electromechanics in the human left ventricle. *MOX report*, 51/2017, 2017.

[29] P. Gervasio, F. Saleri, and A. Veneziani. Algebraic fractional–step schemes with spectral methods for the incompressible Navier–Stokes equations. *Journal of Computational Physics*, 214(1):347–365, 2006.

[30] G. Giantesio and A. Musesti. A continuum model of skeletal muscle tissue with loss of activation. *arXiv preprint arXiv:1701.07823*, 2017.

[31] G. Giantesio and A. Musesti. On the modeling of internal parameters in hyperelastic biological materials. *arXiv preprint arXiv:1609.08651*, 2017.

[32] S.K. Godunov. A difference method for numerical calculation of discontinuous solutions of the equations of hydrodynamics. *Matematicheskii Sbornik*, 89(3):271–306, 1959.

[33] S. Göktepe and E. Kuhl. Electromechanics of the heart: a unified approach to the strongly coupled excitation–contraction problem. *Computational Mechanics*, 45(2-3):227–243, 2010.

[34] A.M. Gordon, A.F. Huxley, and F.J. Julian. The variation in isometric tension with sarcomere length in vertebrate muscle fibres. *The Journal of Physiology*, 184(1):170, 1966.

[35] R.M. Haralick and L.G. Shapiro. Image segmentation techniques. *Computer Vision, Graphics, and Image Processing*, 29(1):100–132, 1985.

[36] E.A. Heidenreich, J.M. Ferrero, M. Doblaré, and J.F. Rodríguez. Adaptive macro finite elements for the numerical solution of monodomain equations in cardiac electrophysiology. *Annals of Biomedical Engineering*, 38(7):2331–2345, 2010.

[37] M. Hirschvogel, M. Bassilious, L. Jagschies, S.M. Wildhirt, and M.W. Gee. A monolithic 3D–0D coupled closed–loop model of the heart and the vascular system: experiment-based parameter estimation for patient–specific cardiac mechanics. *International Journal for Numerical Methods in Biomedical Engineering*, 2017.

[38] B. F. Hoffman and P. F. Cranefield. *Electrophysiology of the Heart.* McGraw-Hill, Blakiston Division, 1960.

[39] G.A. Holzapfel and R.W. Ogden. Constitutive modelling of passive myocardium: a structurally based framework for material characterization. *Philosophical Transactions of the Royal Society of London A: Mathematical, Physical and Engineering Sciences*, 367(1902):3445–3475, 2009.

[40] M.C. Hsu and Y. Bazilevs. Blood vessel tissue prestress modeling for vascular fluid–structure interaction simulation. *Finite Elements in Analysis and Design*, 47(6):593–599, 2011.

[41] P.J. Hunter, M.P. Nash, and G.B. Sands. Computational electromechanics of the heart. *Computational Biology of the Heart*, 12:347–407, 1997.

[42] A. Kamkin, I. Kiseleva, and G. Isenberg. Stretch-activated currents in ventricular myocytes: amplitude and arrhythmogenic effects increase with hypertrophy. *Cardiovascular Research*, 48(3):409–420, 2000.

[43] A.M. Katz. *Physiology of the Heart.* Lippincott Williams & Wilkins, 2010.

[44] S. Land, S.A. Niederer, and N.P. Smith. Efficient computational methods for strongly coupled cardiac electromechanics. *IEEE Transactions on Biomedical Engineering*, 59(5):1219–1228, 2012.

[45] I. LeGrice, P. Hunter, A. Young, and B. Smaill. The architecture of the heart: a data–based model. *Philosophical Transactions of the Royal Society of London A: Mathematical, Physical and Engineering Sciences*, 359(1783):1217–1232, 2001.

[46] J.R. Levick. *An introduction to cardiovascular physiology.* Butterworth-Heinemann, 2013.

[47] C. Luo and Y. Rudy. A model of the ventricular cardiac action potential. Depolarization, repolarization, and their interaction. *Circulation Research*, 68(6):1501–1526, 1991.

[48] C. Luo and Y. Rudy. A dynamic model of the cardiac ventricular action potential. I. Simulations of ionic currents and concentration changes. *Circulation Research*, 74(6):1071–1096, 1994.

[49] M. Munteanu and L.F. Pavarino. Decoupled Schwarz algorithms for implicit discretizations of nonlinear monodomain and bidomain systems. *Mathematical Models and Methods in Applied Sciences*, 19(07):1065–1097, 2009.

[50] D. Nickerson, N. Smith, and P. Hunter. New developments in a strongly coupled cardiac electromechanical model. *EP Europace*, 7(2):118–127, 2005.

[51] F. Nobile, A. Quarteroni, and R. Ruiz-Baier. An active strain electromechanical model for cardiac tissue. *International Journal for Numerical Methods in Biomedical Engineering*, 28(1):52–71, 2012.

[52] D. Noble. A modification of the hodgkinhuxley equations applicable to purkinje fibre action and pacemaker potentials. *The Journal of Physiology*, 160(2):317–352, 1962.

[53] D.A. Nordsletten, S.A. Niederer, M.P. Nash, P.J. Hunter, and N.P. Smith. Coupling multi–physics models to cardiac mechanics. *Progress in Biophysics and Molecular Biology*, 104(1):77–88, 2011.

[54] Raymond W Ogden. *Non-linear elastic deformations.* Courier Corporation, 1997.

[55] L.H. Opie. *Heart physiology: from cell to circulation.* Lippincott Williams & Wilkins, 2004.

[56] S. Pagani. Reduced–order models for inverse problems and uncertainty quantification in cardiac electrophysiology. PhD thesis, Politecnico di Milano, Italy, 2017.

[57] S. Pezzuto. Mechanics of the heart: constitutive issues and numerical experiments. PhD thesis, Politecnico di Milano, Italy, 2013.

[58] S. Pezzuto and D. Ambrosi. Active contraction of the cardiac ventricle and distortion of the microstructural architecture. *International Journal for Numerical Methods in biomedical Engineering*, 30(12):1578–1596, 2014.

[59] M. Potse, B. Dubé, J. Richer, A. Vinet, and R.M. Gulrajani. A comparison of monodomain and bidomain reaction-diffusion models for action potential propagation in the human heart. *IEEE Transactions on Biomedical Engineering*, 53(12):2425–2435, 2006.

[60] A. Quarteroni, T. Lassila, S. Rossi, and R. Ruiz-Baier. Integrated heart - coupling multiscale and multiphysics models for the simulation of the cardiac function. *Computer Methods in Applied Mechanics and Engineering*, 314:345–407, 2017.

[61] A. Quarteroni, A. Manzoni, and C. Vergara. The cardiovascular system: Mathematical modelling, numerical algorithms and clinical applications. *Acta Numerica*, 26:365–590, 2017.

[62] A. Quarteroni, R. Sacco, and F. Saleri. *Numerical Mathematics*, volume 37. Springer Science & Business Media, 2010.

[63] T.A. Quinn and P. Kohl. Combining wet and dry research: experience with model development for cardiac mechano-electric structure-function studies. *Cardiovascular Research*, 97(4):601–611, 2013.

[64] T.G. Reese, R.M. Weisskoff, R.N. Smith, B.R. Rosen, R.E. Dinsmore, and V.J. Wedeen. Imaging myocardial fiber architecture in vivo with magnetic resonance. *Magnetic Resonance in Medicine*, 34(6):786–791, 1995.

[65] F. Regazzoni, L. Dedè, and A. Quarteroni. Active contraction of cardiac cells: a model for sarcomere dynamics with cooperative interactions. *MOX report*, 48/2017, 2017.

[66] B.M. Rocha, B. Lino, R.W. dos Santos, E.M. Toledo, L.P.S. Barra, and J. Sundnes. A two dimensional model of coupled electromechanics in cardiac tissue. In *World Congress on Medical Physics and Biomedical Engineering, September 7-12, 2009, Munich, Germany*, pages 2081–2084. Springer, 2009.

[67] S. Rossi. Anisotropic modeling of cardiac mechanical activation. PhD thesis, EPFL, Switzerland, 2014.

[68] S. Rossi, T. Lassila, R. Ruiz-Baier, A. Sequeira, and A. Quarteroni. Thermodynamically consistent orthotropic activation model capturing ventricular systolic wall thickening in cardiac electromechanics. *European Journal of Mechanics-A/Solids*, 48:129–142, 2014.

[69] S. Rossi, R. Ruiz-Baier, L.F. Pavarino, and A. Quarteroni. Orthotropic active strain models for the numerical simulation of cardiac biomechanics. *International Journal for Numerical Methods in Biomedical Engineering*, 28(6-7):761–788, 2012.

[70] R. Ruiz-Baier, A. Gizzi, S. Rossi, C. Cherubini, A. Laadhari, S. Filippi, and A. Quarteroni. Mathematical modelling of active contraction in isolated cardiomyocytes. *Mathematical Medicine and Biology*, 31(3):259–283, 2014.

[71] Y. Saad. *Iterative Methods for Sparse Linear Systems.* SIAM, 2003.

[72] P.P. Sengupta, J. Korinek, M. Belohlavek, J. Narula, M.A. Vannan, A. Jahangir, and B.K. Khandheria. Left ventricular structure and function. *Journal of the American College of Cardiology*, 48(10):1988–2001, 2006.

[73] J.C. Simo and R.L. Taylor. Quasi-incompressible finite elasticity in principal stretches. continuum basis and numerical algorithms. *Computer Methods in Applied Mechanics and Engineering*, 85(3):273–310, 1991.

[74] R.J. Spiteri and R.C. Dean. On the performance of an Implicit–Explicit Runge–Kutta method in models of cardiac electrical activity. *IEEE Transactions on Biomedical Engineering*, 55(5):1488–1495, 2008.

[75] D.D. Streeter, R.N. Vaishnav, D.J. Patel, H.M. Spotnitz, J. Ross, and E.H. Sonnenblick. Stress distribution in the canine left ventricle during diastole and systole. *Biophysical Journal*, 10(4):345–363, 1970.

[76] S. Sugiura, T. Washio, A. Hatano, J. Okada, H. Watanabe, and T. Hisada. Multi-scale simulations of cardiac electrophysiology and mechanics using the university of tokyo heart simulator. *Progress in Biophysics and Molecular Biology*, 110(2):380–389, 2012.

[77] K. Takizawa, Y. Bazilevs, and T.E. Tezduyar. Space–time and ale-vms techniques for patient-specific cardiovascular fluid–structure interaction modeling. *Archives of Computational Methods in Engineering*, 19(2):171–225, 2012.

[78] K.H.W.J. Ten Tusscher, D. Noble, P.J. Noble, and A.V. Panfilov. A model for human ventricular tissue. *American Journal of Physiology-Heart and Circulatory Physiology*, 286(4):H1573–H1589, 2004.

[79] N.A. Trayanova. Whole-heart modeling applications to cardiac electrophysiology and electromechanics. *Circulation Research*, 108(1):113–128, 2011.

[80] T.P. Usyk, I.J. LeGrice, and A.D. McCulloch. Computational model of three-dimensional cardiac electromechanics. *Computing and Visualization in Science*, 4(4):249–257, 2002.

[81] T.P. Usyk and A.D. McCulloch. Electromechanical model of cardiac resynchronization in the dilated failing heart with left bundle branch block. *Journal of Electrocardiology*, 36:57–61, 2003.

[82] J.A. Vassallo, D.M. Cassidy, J.M. Miller, A.E. Buxton, F.E. Marchlinski, and M.E. Josephson. Left ventricular endocardial activation during right ventricular pacing: effect of underlying heart disease. *Journal of the American College of Cardiology*, 7(6):1228–1233, 1986.

[83] N. Westerhof, J.W. Lankhaar, and B.E. Westerhof. The arterial windkessel. *Medical & Biological Engineering & Computing*, 47(2):131–141, 2009.

[84] J.P. Whiteley. An efficient numerical technique for the solution of the monodomain and bidomain equations. *Biomedical Engineering, IEEE Transactions on*, 53(11):2139–2147, 2006.

[85] A.Y.K. Wong and P.M. Rautaharju. Stress distribution within the left ventricular wall approximated as a thick ellipsoidal shell. *American Heart Journal*, 75(5):649–662, 1968.

[86] J. Wong and E. Kuhl. Generating fibre orientation maps in human heart models using poisson interpolation. *Computer Methods in Biomechanics and Biomedical Engineering*, 17(11):1217–1226, 2014.

[87] F.C.P. Yin, R.K. Strumpf, P.H. Chew, and S.L. Zeger. Quantification of the mechanical properties of noncontracting canine myocardium under simultaneous biaxial loading. *Journal of Biomechanics*, 20(6):577–589, 1987.

MOX Technical Reports, last issues

Dipartimento di Matematica
Politecnico di Milano, Via Bonardi 9 - 20133 Milano (Italy)

26/2018 Vergara, C.; Zonca, S.
Extended Finite Elements method for fluid-structure interaction with an immersed thick non-linear structure

27/2018 Antonietti, P.F.; Verani, M.; Vergara, C.; Zonca, S.
Numerical solution of fluid-structure interaction problems by means of a high order Discontinuous Galerkin method on polygonal grids

25/2018 Chave, F.; Di Pietro, D.A.; Formaggia, L.
A Hybrid High-Order method for passive transport in fractured porous media

24/2018 Bassi, C.; Abbà, A.; Bonaventura,L.; Valdettaro,L.
Direct and Large Eddy Simulation of three-dimensional non-Boussinesq gravity currents with a high order DG method

23/2018 Benacchio, T.;Bonaventura,L.
A seamless extension of DG methods for hyperbolic problems to unbounded domains

22/2018 Pegolotti, L.; Dede', L.; Quarteroni, A.
Isogeometric Analysis of the electrophysiology in the human heart: numerical simulation of the bidomain equations on the atria

21/2018 Gervasio, P.; Dede', L.; Chanon, O.; Quarteroni, A.
Comparing Isogeometric Analysis and Spectral Element Methods: accuracy and spectral properties

20/2018 Bassi, C. ; Abbà, A.; Bonaventura L.; Valdettaro, L.
A priori tests of a novel LES approach to compressible variable density turbulence

19/2018 Menghini, F.; Dede', L.; Quarteroni, A.
Variational Multiscale LES modeling of blood flow in an idealized left human heart

18/2018 Antonietti, P.F.; Bonaldi, F.; Mazzieri, I.
A high-order discontinuous Galerkin approach to the elasto-acoustic problem